# Ekman decay of monopolar vortices on a topographic Beta-plane

Custers, B.H.M.

*Award date:*
2000

Technische Universiteit Eindhoven

Faculteit Technische
Natuurkunde
Groep Transportfysica
Gebouw Cascade
Postbus 513
5600 MB Eindhoven

Titel:

# Ekman decay of monopolar vortices on a topographic $\beta$-plane

Auteur: B.H.M. Custers

Verslagnr: R-1498-A

Datum: February 2000

Capaciteitsgroep : Werveldynamica
Begeleiders : L. Zavala Sansón MSc.
Prof. dr. ir. G.J.F. van Heijst

# Abstract

In this thesis the evolution and decay of non-isolated monopolar vortices on a topographic $\beta$-plane has been studied. This was done by performing both laboratory experiments and numerical simulations (based on two-dimensional physical models). Laboratory experiments were carried out in a rotating tank system, in which vortices were created by withdrawing a certain amount of fluid. The topographic $\beta$-plane consists of a linear sloping bottom on which the vortex drifts to the 'north-west', while gradually decaying. This decay is associated with bottom friction (Ekman effects) and with Rossby wave radiation, due to the $\beta$-effect.

Experiments were done with different water depths. It was found that the lower the water depth, the faster the vortex decay. The basic reason for this is that bottom friction effects are more effective for lower water depths. It was shown that the experimental vortices can be numerically simulated by using a two-dimensional model with Ekman friction and a variable topography. The calculated Ekman times and the trajectories of the vortices were similar in the experiments and simulations, indicating that the model on which the simulations are based is able to simulate the bottom friction due to the Ekman layer on a topographic $\beta$-plane. The decay of the peak vorticity on the topographic $\beta$-plane can be described in the same fashion as the flat bottom case, but at a different rate. Ekman times associated with the sloping bottom were found to be approximately half of those associated with the flat topography. The influence of the topographic $\beta$-plane was examined by performing simulations on a flat bottom. In the case of the topographic $\beta$-plane Ekman times are about 55 % of those in the case of the flat bottom, as expected. Two reasons for this considerably faster decay are the creation of Rossby waves and the squeezing of the vortex as it drifts to the north. In order to examine the influence of bottom friction due to the Ekman layer, simulations without Ekman effects were performed. The vortex decay showed to be considerably slower, indicating the importance of bottom friction. The vortices leak fluid from the north-eastern part due to squeezing effects as fluid columns move upslope in the cyclonic motion. The curved north-westward trajectories of the vortices were partially explained by the released fluid to the ambient. Passive tracers in the simulations showed similar behaviour.

# Contents

# Chapter 1

# Introduction

Fluid dynamics is the research field that studies the phenomena of liquids and gases. Geophysical fluid dynamics is the part of fluid dynamics that focuses on large-scale flows in the atmosphere and in oceans. Two effects are typical for geophysical fluid dynamics: the presence of background rotation and the stratification of fluids. In this report the effects of the latter, the stratification, will not be treated.

The importance of geophysical fluid dynamics can be found in several examples, like predicting the spreading of pollutants, the prediction of the paths of hurricanes, the understanding of the global climate and the prediction of the weather.

The presence of background rotation is due to the spin of the Earth around its axis. This rotation produces two extra forces that are not present in a non-rotating system: the centrifugal force and the Coriolis force. The former plays no important role in geophysical motions, because it can be included together with the gravitational force. The latter has only a significant effect on the flow when the timescale of motion is bigger than the rotation period of the Earth. This criterion is often used in geophysical fluid dynamics to define a large-scale motion.

A characteristic feature in fluid dynamics is a coherent vortex, or eddy. Vortices are closed circulations that are relatively persistent [1]. A cyclone is a vortex whose rotation is in the same sense as the background rotation, i.e., for geophysical flows, counterclockwise in the Northern Hemisphere; an anticyclone rotates in the opposite sense. Vortices are present in several different forms with different properties. For an overview and description of

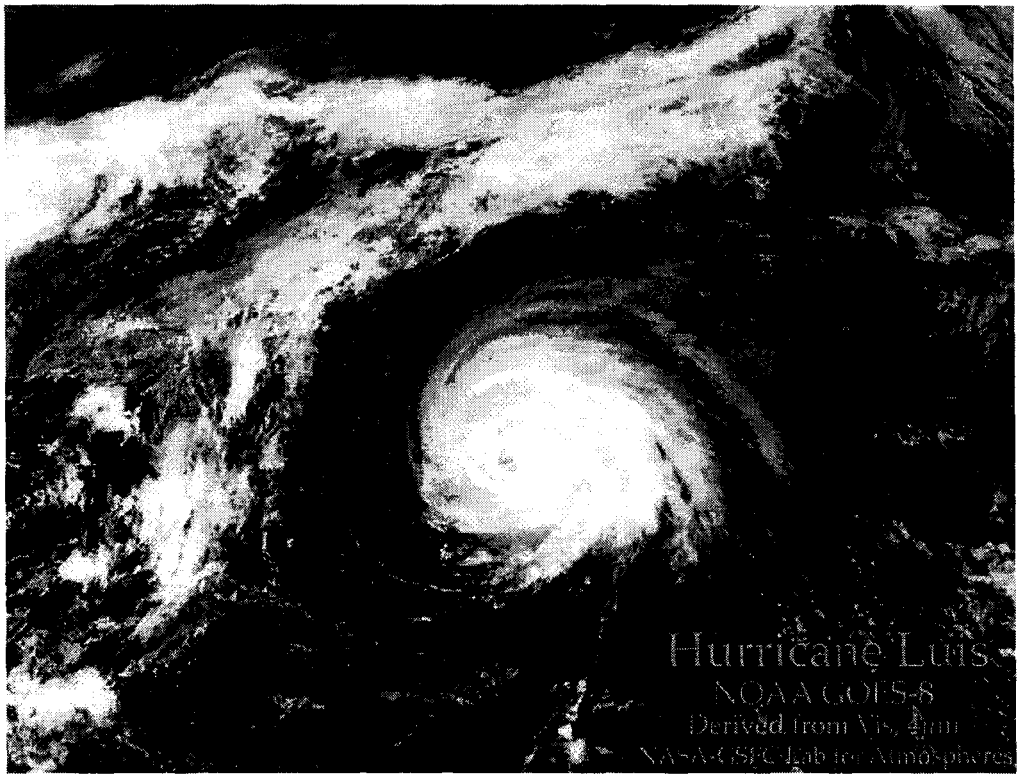


Figure 1.1: *Hurricane Luis, at the coast of Florida at September 6 1995. Maximum winds are about 233 km/h. Satellite photo taken by NASA-GSFC Laboratory for Atmospheres*

the most common vortices, see [2]. In a so-called monopolar vortex, the fluid moves around one centre. Some of the most well-known examples of vortices in the atmosphere are low-pressure areas on weather maps. The dimensions of oceanic vortices can be 10 to 100 km, and they can exist up to several years. Atmospheric vortices, in contrast, persist only for days or weeks. In figure 1.1 a spectacular example of an atmospheric vortex, a hurricane, is shown.

The Coriolis force is dependent on the latitude. For not too large scales (<1000 km) the latitudinal variation of the Coriolis force can be linearized around some reference latitude. This is called the $\beta$-plane approximation. In the laboratory this situation can be simulated with a rotating tank with a lin-

early sloping bottom, as described in chapter 3. Such a configuration is called the topographic $\beta$-plane and is a fundamental tool in this report. Monopolar vortices in the Northern Hemisphere move in the north-western direction on a $\beta$-plane when they are cyclonic and in the south-western direction when they are anticyclonic [3].

Geophysical flows can be considered as nearly two-dimensional because their horizontal length scales are much larger than their vertical length scales. However, when surface and bottom friction are included by means of so-called Ekman boundary layers, the two-dimensional motion is slightly broken. Thus, it can be said that geophysical flows have a quasi-two-dimensional character. Although these Ekman layers at the surface and at the bottom of the flow are very thin compared to the vertical length scales, they cause some weak damping effects. One of these effects is the exchange of fluid between the boundary layer and the interior of the flow. This effect is called Ekman-pumping and causes the decay of the flow field. In this report only bottom friction effects will be considered.

A two-dimensional model for the Ekman decay of monopolar vortices on a flat bottom is described and tested in [4]. A more general formulation for rotating barotropic flows over a variable topography is derived in [5], by including nonlinear Ekman terms in the vorticity equation. According to this model Ekman effects are enhanced in shallow layers.

This report deals with Ekman decay of monopolar vortices on a topographic $\beta$-plane. With experiments and numerical simulations the model described in [5] was tested.

More detailed information on the underlying theories can be found in chapter 2. A description of the experimental arrangement is given in chapter 3. Chapter 4 shows the experimental results. Afterwards, the experiments were reproduced by means of numerical simulations, using the program NSEVOL which solves the two-dimensional Navier-Stokes equations in the vorticity-streamfunction formulation [6]. The results of these numerical simulations can be found in chapter 5. A discussion of the results and the conclusions of this study are presented in chapter 6.

# Chapter 2

# Theory

## 2.1 Background rotation

In geophysical flows, the background rotation is related with the rotation of the Earth around its own axis. This rotation produces two extra forces, not present in the non-rotating case: the centrifugal force and the Coriolis force. As already mentioned in the Introduction, in most cases only the Coriolis effects are important.

Before describing the influence of the Coriolis force, it is useful to introduce a reference framework rotating with the planet. We use a local Cartesian coordinate system. The $x$-axis is directed to the east, the $y$-axis is directed to the north and the $z$-axis is upward (see figure 2.1).

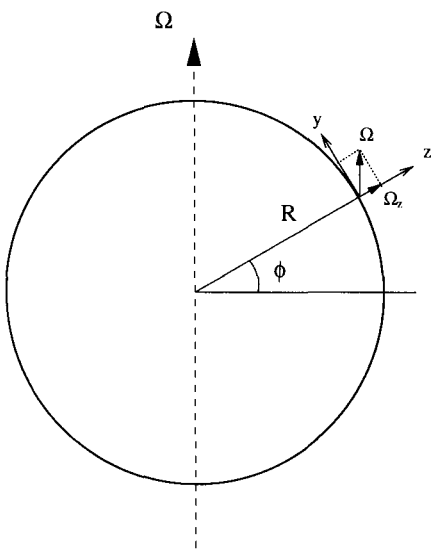


Figure 2.1: *The coordinates defined on a rotating sphere*

The oceans and the atmosphere can be considered as thin layers where fluid motion is predominantly horizontal (two-dimensional), i.e. parallel to the Earth's surface. Thus, the vorticity vector of geophysical flows is aligned with the vertical direction, perpendicular to the surface, i.e. in the $z$-direction. The dependence of the Coriolis force on the latitude $\phi$ is represented by the so-called Coriolis parameter $f$, which is defined as:

$$f = 2\Omega \sin \phi \tag{2.1}$$

with $\Omega$ the planetary angular velocity. In the Northern Hemisphere $f$ is positive, while it is zero at the equator and negative in the Southern Hemisphere.

## 2.2 Potential vorticity

Balance of momentum for a fluid in a rotating coordinate framework is described by the Navier-Stokes equation:

$$\frac{\partial \underline{v}}{\partial t} + (\underline{v} \cdot \nabla)\underline{v} + 2\underline{\Omega} \times \underline{v} = -\frac{1}{\rho}\nabla P + \nu \nabla^2 \underline{v} \tag{2.2}$$

with P the reduced pressure, defined by:

$$P = p - \rho \Phi_{grav} - \frac{1}{2}\rho \Omega^2 r^2 \tag{2.3}$$

where $\rho$ is the fluid density, which is assumed to be constant for all situations in this report. $\underline{v}$ is the velocity vector $(u,v,w)$, $p$ is the pressure, $t$ is the time, $r$ is the radial distance to the rotation axis and $\nu$ is the kinematic viscosity, which is also assumed to be constant. The gravitational ($\Phi_{grav}$) and the centrifugal ($\frac{1}{2}\Omega^2 r^2$) potentials are such that $\nabla(\Phi_{grav} + \frac{1}{2}\Omega^2 r^2) = \underline{g} = (0,0,-g)$, with $g$ the constant gravity acceleration. The Coriolis acceleration is represented by $2\underline{\Omega} \times \underline{v}$.

When the horizontal length scale L is much larger than the depth scale D, i.e. D $\ll$ L (see figure 2.2) and neglecting all geometrical terms associated with the Earth's curvature, the $x$-, $y$- and $z$-components of (2.2) are:

$$\frac{\partial u}{\partial t} + u\frac{\partial u}{\partial x} + v\frac{\partial u}{\partial y} + w\frac{\partial u}{\partial z} - fv = -\frac{1}{\rho}\frac{\partial p}{\partial x} + \nu \nabla^2 u \tag{2.4}$$

$$\frac{\partial v}{\partial t} + u\frac{\partial v}{\partial x} + v\frac{\partial v}{\partial y} + w\frac{\partial v}{\partial z} + fu = -\frac{1}{\rho}\frac{\partial p}{\partial y} + \nu \nabla^2 v \tag{2.5}$$

$$\frac{\partial w}{\partial t} + u\frac{\partial w}{\partial x} + v\frac{\partial w}{\partial y} + w\frac{\partial w}{\partial z} = -\frac{1}{\rho}\frac{\partial p}{\partial z} - g + \nu \nabla^2 w \tag{2.6}$$

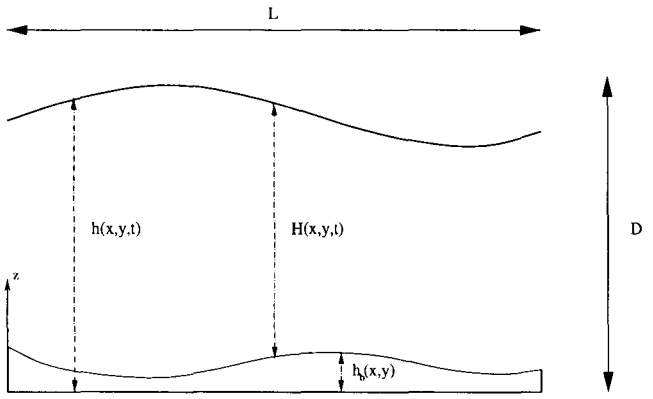


Figure 2.2: *The shallow water model*

Using the shallow water approximation (D $\ll$ L) the vertical accelerations and viscous effects can be neglected in equation 2.6 [7]. The result is the hydrostatic approximation:

$$\frac{1}{\rho}\frac{\partial p}{\partial z} = -g \tag{2.7}$$

After vertical integration this becomes:

$$p = \rho g(h - z) + p_0 \tag{2.8}$$

with $h$ the water height above the reference level $z = 0$ (see figure 2.2) and $p_0$ the pressure at the fluid surface. When $p_0$ is assumed to be constant, the components of the horizontal pressure gradient are given by:

$$\frac{\partial p}{\partial x} = \rho g \frac{\partial h}{\partial x} \tag{2.9}$$

$$\frac{\partial p}{\partial y} = \rho g \frac{\partial h}{\partial y} \tag{2.10}$$

Assuming the horizontal velocities as $z$-independent (since the horizontal pressure gradients are so) and considering an inviscid fluid, the horizontal momentum equations (2.4) and (2.5) become:

$$\frac{\partial u}{\partial t} + u\frac{\partial u}{\partial x} + v\frac{\partial u}{\partial y} - fv = -g\frac{\partial h}{\partial x} \tag{2.11}$$

$$\frac{\partial v}{\partial t} + u\frac{\partial v}{\partial x} + v\frac{\partial v}{\partial y} + fu = -g\frac{\partial h}{\partial y} \tag{2.12}$$

Taking the $y$-derivative of (2.11), the $x$-derivative of (2.12), and subtracting them from each other results in:

$$\frac{d(\zeta + f)}{dt} + (\zeta + f)\left(\frac{\partial u}{\partial x} + \frac{\partial v}{\partial y}\right) = 0 \tag{2.13}$$

where $\zeta$ is the relative vorticity:

$$\zeta = \frac{\partial v}{\partial x} - \frac{\partial u}{\partial y} \tag{2.14}$$

and with d/dt the material derivative, defined by:

$$\frac{d}{dt} = \frac{\partial}{\partial t} + u\frac{\partial}{\partial x} + v\frac{\partial}{\partial y} \tag{2.15}$$

The sum of the relative vorticity $\zeta$ and the planetary vorticity $f$ is called the absolute vorticity. Equation (2.13) expresses that a positive divergence of the flow field implies a decreasing absolute vorticity per fluid column. A negative divergence causes an increase of absolute vorticity. The vertically integrated two-dimensional continuity equation is given by:

$$\frac{dH}{dt} + \frac{\partial(Hu)}{\partial x} + \frac{\partial(Hv)}{\partial y} = 0 \tag{2.16}$$

Using this, equation (2.13) can be rewritten in terms of the water depth $H$:

$$\frac{d}{dt}\left(\frac{\zeta + f}{H}\right) = 0 \tag{2.17}$$

This expresses conservation of the so-called potential vorticity $\frac{\zeta+f}{H}$ . The potential vorticity can analogously be defined for laboratory experiments.

## 2.3 The $\beta$-plane

When considering small scale motions ( $<$ 100 km), $f$ may be assumed to be constant:

$$f = f_0 = 2\Omega \sin \phi_0 \tag{2.18}$$

with $\phi_0$ the reference latitude. This is commonly referred to as the $f$-plane approximation.

For larger length scales the latitudinal variation in $f$ is better represented by expanding the Coriolis parameter in a Taylor series around $\phi_0$:

$$f(\phi) = f(\phi_0 + \delta\phi) = 2\Omega[\sin \phi_0 + \frac{\cos \phi_0}{R} R\delta\phi + O(\delta\phi^2)] \tag{2.19}$$

Writing $R\delta\phi = y$ and with the assumption that quadratic and higher order terms can be neglected, this can be expressed as:

$$f = f_0 + \beta y \tag{2.20}$$

where the new constant given by $\beta = 2\Omega\cos\phi_0/R$ has been introduced. This linearisation is usually referred to as the $\beta$-plane approximation (see figure 2.3).

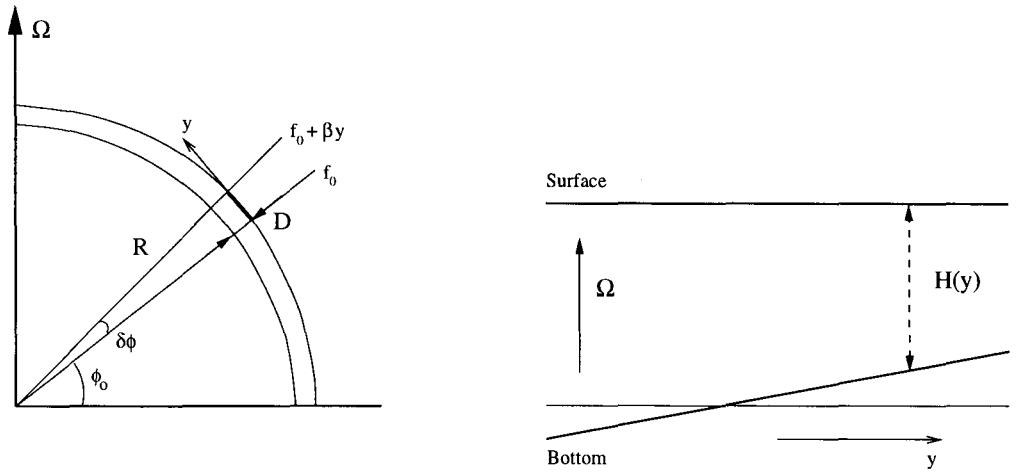


Figure 2.3: *Left: linearisation of $f(\phi)$ results in the $\beta$-plane approximation. Right: Laboratory simulation of the latitudinal variation of $f(\phi)$ by the principle of conservation of potential vorticity*

The $\beta$-plane is a useful approximation when length scales of motion are of order 100 to 1000 km, i.e. when weak $f$ variations have to be taken into account. Note that for a fluid parcel in an ocean or atmosphere over a flat bottom topography ($H = H_0$) equation (2.17) implies:

$$\zeta = cH_0 - f_0 - \beta y \tag{2.21}$$

where $c$ is a constant. The $\beta$-effect can be simulated in the laboratory by using a rotating tank with a linear bottom topography in the $y$-direction (see figure 2.3). According to [13] equation (2.17) then becomes:

$$\zeta = cH(y) - f_0 \tag{2.22}$$

where $c$ is a constant and $f_0 = 2\Omega$, with $\Omega$ the angular velocity of the tank. This type of bottom topography in the rotating tank is called the 'topographic $\beta$-plane'. The resemblance between the laboratory and the planetary situation is the following: a northward shift (increasing $y$) in the planetary situation means a reduction of relative vorticity. In the laboratory situation a shift to the shallow part of the tank causes a reduction of the relative vorticity. Thus the shallow part of the tank corresponds to the north. Similarly, the deep part of the tank corresponds to the south.

## 2.4 Motion of a monopole

On an $f$-plane (i.e. without any topography in the rotating tank) a monopolar circular vortex remains at a fixed position. The basic reason is that there are no asymmetrical changes in relative vorticity of fluid columns (free surface variations are being ignored) able to induce motion on the monopole. On a topographic $\beta$-plane the situation is entirely different. Consider for instance a cyclonic monopole (see figure 2.4).

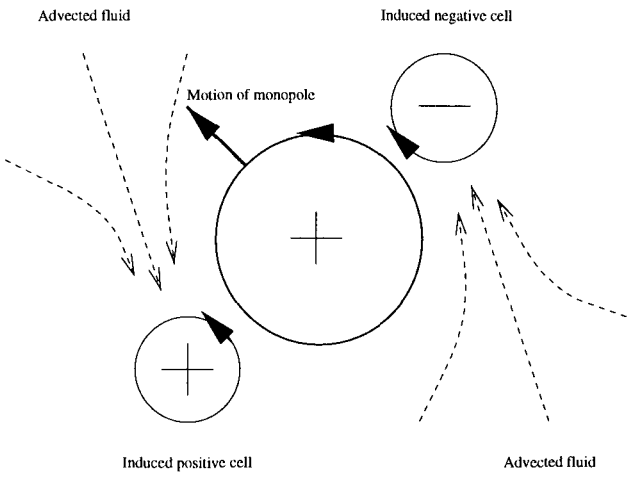


Figure 2.4: *A positive monopolar vortex on the $\beta$-plane: advection of fluid particles results in a positive cell in the south-western side of the vortex and a negative cell in the north-east. Both cells induce the vortex motion in the north-western direction.*

At the western side the vortex advects fluid from north to south, which acquires positive relative vorticity, according to equation (2.17). At the eastern side the vortex advects fluid parcels that move from south to north, resulting in negative relative vorticity. The negative cell in the north-east and the positive cell in the south-west will induce the vortex drift in the north-west direction.

Applying similar arguments for an anticyclonic monopole, the resulting motion is to the south-west.

## 2.5 Ekman layers

Until now viscous effects have not been taken into account. Although the motion in the bulk of a finite flow domain may be considered as inviscid, this approximation is no longer valid near the domain boundaries. The effects of viscous forces near boundaries are taken into account by means of boundary layers. In this report only the bottom boundary layer, the so-called Ekman layer, is considered, while the effects of lateral walls will be assumed negligible.

To express the ratio of the viscous force and the Coriolis force we use the so-called Ekman number:

$$\mathrm{E} = \frac{\nu}{\Omega H^2} \tag{2.23}$$

where $\nu$ is the kinematic viscosity and $H$ is the depth scale of motion. The non-dimensional thickness $d$ of the Ekman layer is given by:

$$d = \sqrt{E} \tag{2.24}$$

The physical thickness of the Ekman layer is given by $d_E = Hd = HE^{1/2} = (\nu/\Omega)^{1/2}$, which is generally very small in a rapidly-rotating, slightly viscous fluid.

Consider the Ekman layer under a uniform, geostrophic flow in a homogeneous fluid over a flat bottom (see figure 2.5).

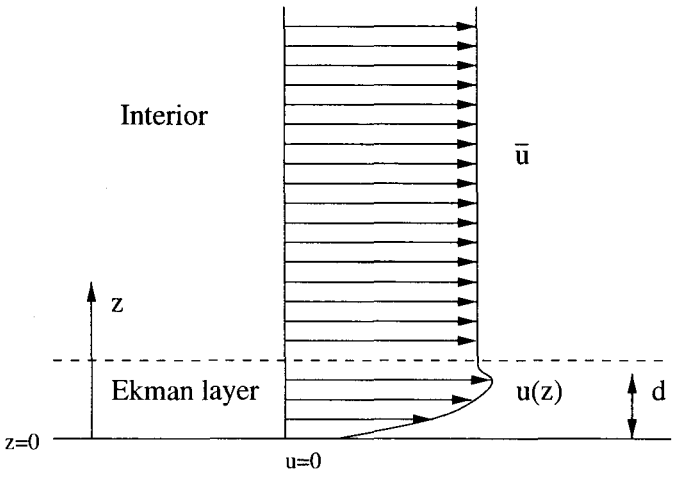


Figure 2.5: *The influence of the friction of a flat bottom on a uniform flow*

Since there is no horizontal divergence, the continuity equation yields $\partial w/\partial z = 0$. Assuming that the Rossby number is small (i.e. $U < \Omega L$), the non-linear terms in equations (2.4) through (2.6) can be neglected [1]. For the case of stationary flow inside the Ekman layer, equations (2.4) - (2.6) can be reduced to:

$$-fv = -\frac{1}{\rho}\frac{\partial p}{\partial x} + \nu\frac{\partial^2 u}{\partial z^2} \tag{2.25}$$

$$fu = -\frac{1}{\rho}\frac{\partial p}{\partial y} + \nu\frac{\partial^2 v}{\partial z^2} \tag{2.26}$$

$$g = -\frac{1}{\rho}\frac{\partial p}{\partial z} \tag{2.27}$$

Note that due to the shallow water approximation the horizontal second derivatives of the velocity components have been neglected in the viscous terms. Also it is assumed that the hydrostatic balance applies. Since the velocity of the main flow is $\overline{u}$ = (U, 0, 0), outside the boundary layer the equations (2.25) and (2.26) become

$$0 = -\frac{1}{\rho}\frac{\partial p_I}{\partial x} \tag{2.28}$$

$$fU = -\frac{1}{\rho}\frac{\partial p_I}{\partial y} \tag{2.29}$$

By taking the horizontal derivative of equation (2.27) it follows that the horizontal pressure gradient is independent of $z$, so that (2.28) and (2.29) are valid for all $z$. Assuming that the pressure in the Ekman layer is equal to that in the interior flow ($p \approx p_I$) and thus combining equations (2.25) with (2.28) and (2.26) with (2.29) respectively, we obtain:

$$-fv = \nu\frac{d^2u}{dz^2} \tag{2.30}$$

$$f(u - U) = \nu\frac{d^2v}{dz^2} \tag{2.31}$$

The solution of this system, when applying the correct boundary conditions ($\overline{u}$=0 at the bottom and $\overline{u}$=(U, 0, 0) far in the interior of the flow), are:

$$u = U(1 - e^{-z/d_E}\cos\frac{z}{d_E}) \tag{2.32}$$

$$v = Ue^{-z/d_E}\sin\frac{z}{d_E} \tag{2.33}$$

where $d_E$ is the Ekman layer thickness. In figure 2.6 the profiles of the horizontal velocity components $u$ and $v$ are shown, together with their projections on the horizontal plane (a so-called hodograph). From the hodograph it can be seen that the velocity vector at the bottom is turned 45° to the left of the current outside the Ekman layer.

For spatially non-uniform interior flows, the horizontal divergence is different from zero inside the Ekman layer. As a consequence, fluid is exchanged between the boundary layer and the interior. This effect is called Ekman-pumping. The vertical velocity $w_I$ in the interior flow caused by Ekman-pumping is given by [8]:

$$w_I(x, y) = \frac{1}{2}E^{1/2}\omega_I\,, \quad z = 0 \tag{2.34}$$

Note that the Ekman suction depends on the vorticity of the geostrophic flow ($\omega_I$).

This effect causes the decay of the flow field. For instance, a cyclonic vortex ($\omega_I > 0$ and therefore $w_I > 0$) will be squeezed by fluid from the Ekman layer and thus it will lose absolute vorticity. An anticyclonic vortex, in contrast, will be stretched and therefore it will also decay.

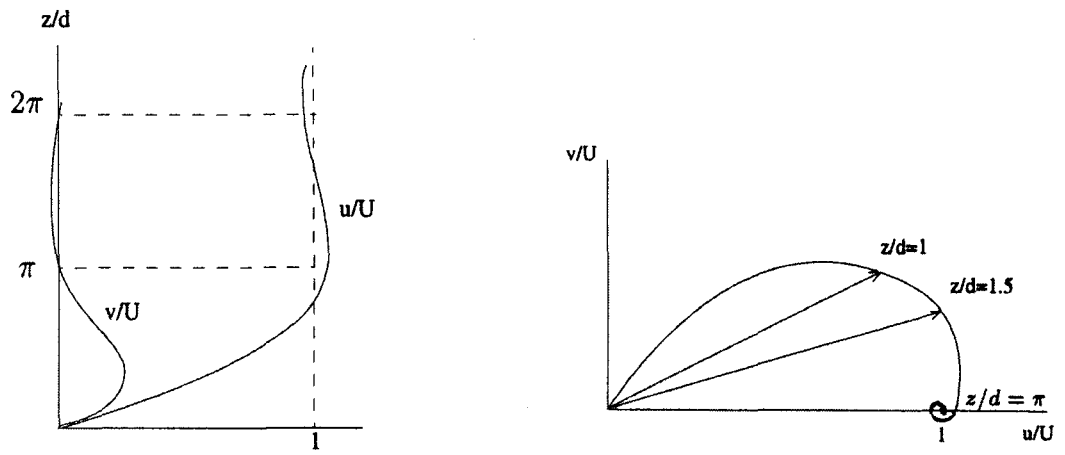


Figure 2.6: *Left: the velocity profiles of u and v in the Ekman layer. Right: the hodograph, the projection of u and v on the horizontal plane. Figure from [15]*

## 2.6 The vorticity equation

Consider the horizontal components of the Navier-Stokes equations (2.4) and (2.5) in two dimensions ($w$=0). The pressure gradients can be eliminated by taking the $y$-derivative of (2.4) and subtracting it from the $x$-derivative of (2.5). This results in the vorticity equation:

$$\frac{\partial \zeta}{\partial t} + u\frac{\partial \zeta}{\partial x} + v\frac{\partial \zeta}{\partial y} + \left(\frac{\partial u}{\partial x} + \frac{\partial v}{\partial y}\right)(\zeta + f) = \nu \nabla^2 \zeta \tag{2.35}$$

with $\zeta$ the relative vorticity, given by equation (2.14). For a two-dimensional flow over a flat bottom and no Ekman friction, the continuity equation is given by:

$$\frac{\partial u}{\partial x} + \frac{\partial v}{\partial y} = 0 \tag{2.36}$$

Now we introduce the stream function $\psi$ defined by:

$$\begin{cases} u = \dfrac{\partial \psi}{\partial y} \\ v = -\dfrac{\partial \psi}{\partial x} \end{cases} \tag{2.37}$$

Using this definition and the continuity equation we can rewrite equation (2.35):

$$\frac{\partial \zeta}{\partial t} + J(\zeta, \psi) = \nu \nabla^2 \zeta \tag{2.38}$$

with J the Jacobian, defined by:

$$J(\zeta, \psi) = \frac{\partial \zeta}{\partial x}\frac{\partial \psi}{\partial y} - \frac{\partial \psi}{\partial x}\frac{\partial \zeta}{\partial y} \tag{2.39}$$

Inserting equation (2.37) in the definition of the relative vorticity (2.14) it is verified that:

$$\zeta = -\nabla^2 \psi \tag{2.40}$$

Thus, $\zeta$ and $\psi$ have to fulfil a Poisson equation.

For the case of a variable bottom topography $H(x, y)$, the two-dimensional model given by (2.38) and (2.40) can be extended, starting with the new continuity equation, given by:

$$\frac{\partial (Hu)}{\partial x} + \frac{\partial (Hv)}{\partial y} = 0 \tag{2.41}$$

i.e. equation (2.16) without temporal variations of the depth field (the so-called rigid-lid approximation). Now a new stream function is defined, such that:

$$\begin{cases} Hu = & \dfrac{\partial \psi_p}{\partial y} \\ Hv = -\dfrac{\partial \psi_p}{\partial x} \end{cases} \tag{2.42}$$

The new vorticity equation, in terms of the stream function $\psi_p$ then becomes:

$$\frac{\partial \zeta}{\partial t} + J(\omega_p, \psi_p) = \nu \nabla^2 \zeta \tag{2.43}$$

with $\omega_p$ the potential vorticity:

$$\omega_p = \frac{\zeta + f}{H} \tag{2.44}$$

The relation between the relative vorticity and the streamfunction is:

$$\zeta = -\frac{1}{H}\nabla^2 \psi_p + \frac{1}{H^2}\nabla H \cdot \nabla \psi_p \tag{2.45}$$

This modified Poisson equation reduces to equation (2.40) when there are no topography variations ($\nabla H$=0 and $\psi_p = H\psi$).

In [5] the model given by (2.43) and (2.45) is even further extended in order to incorporate Ekman effects from the bottom. A detailed derivation can be found in appendix B. The model is given by:

$$\frac{\partial \zeta}{\partial t} + J(\omega_p, \psi_p) - \frac{d_E}{2H}\nabla\psi_p \cdot \nabla\omega_p = \nu\nabla^2\zeta - \frac{d_E}{2H}\zeta(\zeta + f) \tag{2.46}$$

$$\zeta = -\frac{1}{H}\nabla^2\psi_p + \frac{1}{H^2}\nabla H \cdot \nabla\psi_p + \frac{d_E}{2H}\frac{2}{H^2}J(H, \psi_p) \tag{2.47}$$

In these equations $d_E$ is the Ekman layer thickness, given by $d_E = HE^{1/2}$. This model can be reduced to (2.43) and (2.45) by ignoring bottom friction effects ($d_E$=0).

The model given by (2.46) and (2.47) can also be reduced to the case of a flat bottom, incorporating bottom friction ($H$=$H_0$=constant, $\nabla H = 0$ and $\psi_p = H\psi$ again; see also [4]):

$$\frac{\partial \zeta}{\partial t} + J(\zeta, \psi) - \frac{d_E}{2H_0}\nabla\psi \cdot \nabla\zeta = \nu\nabla^2\zeta - \frac{d_E}{2H_0}\zeta(\zeta + f) \tag{2.48}$$

$$\zeta = -\nabla^2\psi \tag{2.49}$$

An overview of all models described in this section is given in table 2.1:

| | Flat bottom | Topography |
|---|---|---|
| No friction | Model 1<br>(2.38), (2.40) | Model 2<br>(2.43), (2.45) |
| Friction | Model 3<br>(2.48), (2.49) | Model 4<br>(2.46),(2.47) |

Table 2.1: *Overview of the two-dimensional physical models with and without friction and/or bottom topography variations*

# Chapter 3

# Experimental set-up

## 3.1 Rotating tank

In order to simulate the latitudinal variation of the Coriolis parameter $f$ in the laboratory, a rotating tank with a sloping bottom is used (see figure 3.1). On this topographic $\beta$-plane, the shallow part corresponds to the north, as explained in section 2.3. The rectangular tank has dimensions 100 x 150 $cm$ and rotates at 0.5 $rad/s$ in anticlockwise direction. The slope of the bottom was taken 8 $cm$ over the length of 100 $cm$. For the different experiments the maximum water depth was varied: $H$=12, 18 and 24 $cm$.

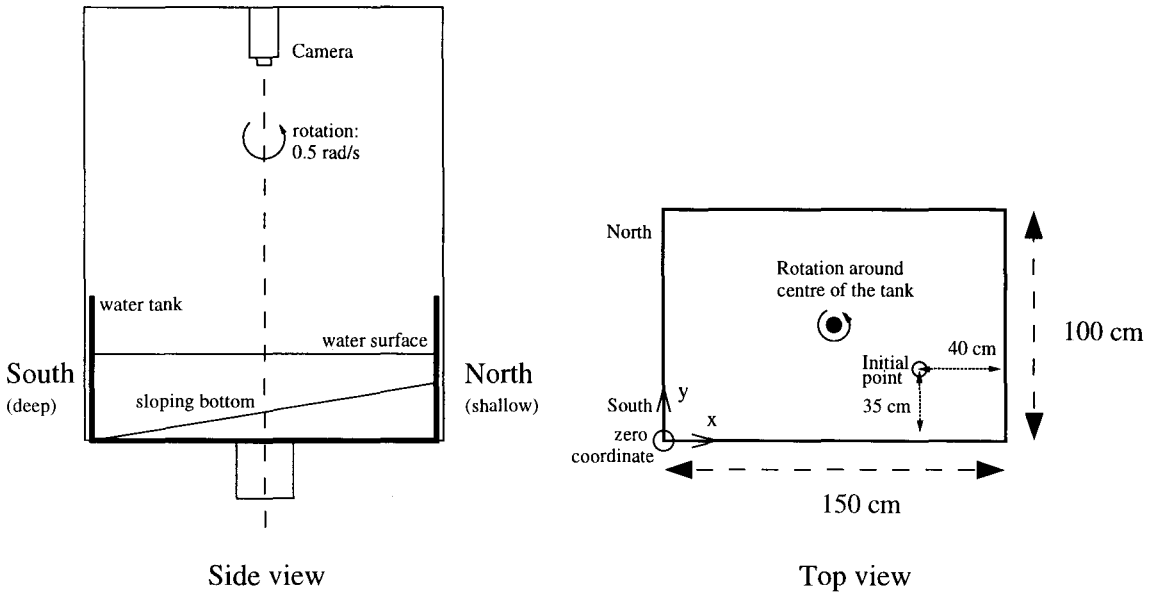


Figure 3.1: *Rotating tank: side and top view*

The tank has to rotate about 30 to 40 minutes before the experiments can be started in order to let the water reach a state of solid body rotation. A camera is placed above, co-rotating with the tank, to record the experiments on video tape. On all sides of the tank strip lights were placed to get a homogeneous and bright light over the water surface.

The $\beta$-value in the laboratory situation is given by [13]:

$$\beta = \frac{fs}{Hl} \tag{3.1}$$

with $s$ the maximum height of the sloping bottom and $l$ the length of the tank in the direction of the sloping bottom. In all laboratory experiments $s = 8\ cm$ and $l = 100\ cm$, while $f_0 = 1s^{-1}$. The calculated values for $\beta$ are shown in table 3.1.

The $\beta$-values for the ocean and the laboratory can be compared by introducing the following non-dimensional number [1]:

$$\beta' = \frac{\beta R}{f_0} \tag{3.2}$$

with R the horizontal length scale of interest, for instance, the vortex radius. For mid-latitudes in the ocean, typical values for $\beta$, $R$ and $f_0$ are $2 \cdot 10^{-11}\ m^{-1}\ s^{-1}$, $10^5\ m$ and $10^{-4}\ s^{-1}$ respectively [14]. This results in a value of $\beta'$=0.02. On the other hand, using typical experimental values of $\beta$, $R$ and $f_0$ yields $\beta' \approx 0.02$, which is of the same order of magnitude than the oceanic case. The $\beta$-effect, therefore, is similar in the experiments and the ocean.

| Experiment | H $(m)$ | $\beta$ $(m^{-1}s^{-1})$ | R $(m)$ |
|---|---|---|---|
| 1 | 0.12 | 0.67 | 0.03 |
| 2 | 0.18 | 0.44 | 0.04 |
| 3 | 0.24 | 0.33 | 0.05 |

Table 3.1: *Experimental parameters*

## 3.2 Monopoles

The cyclonic monopolar vortices used in the experiments were created by locally withdrawing a fixed amount of fluid. This is done by syphoning some water through a thin tube that is perforated along the full depth. The created vortex is called a 'sink vortex'.

The approximate expression for the velocity profile is given by [3]:

$$v_{sink}(r) = \frac{\sigma^2 \mu}{r}(1 - e^{-\frac{r^2}{2\sigma^2}}) \tag{3.3}$$

with $\mu$ the peak vorticity, $\sigma$ the horizontal length scale and $r$ the distance to the centre of the vortex. The corresponding vorticity distribution is given by:

$$\zeta_{sink}(r) = \mu e^{-\frac{r^2}{2\sigma^2}} \tag{3.4}$$

Figure 3.2 shows the vorticity profile (3.4) and the corresponding azimuthal velocity profile (3.3) of the sink vortex.

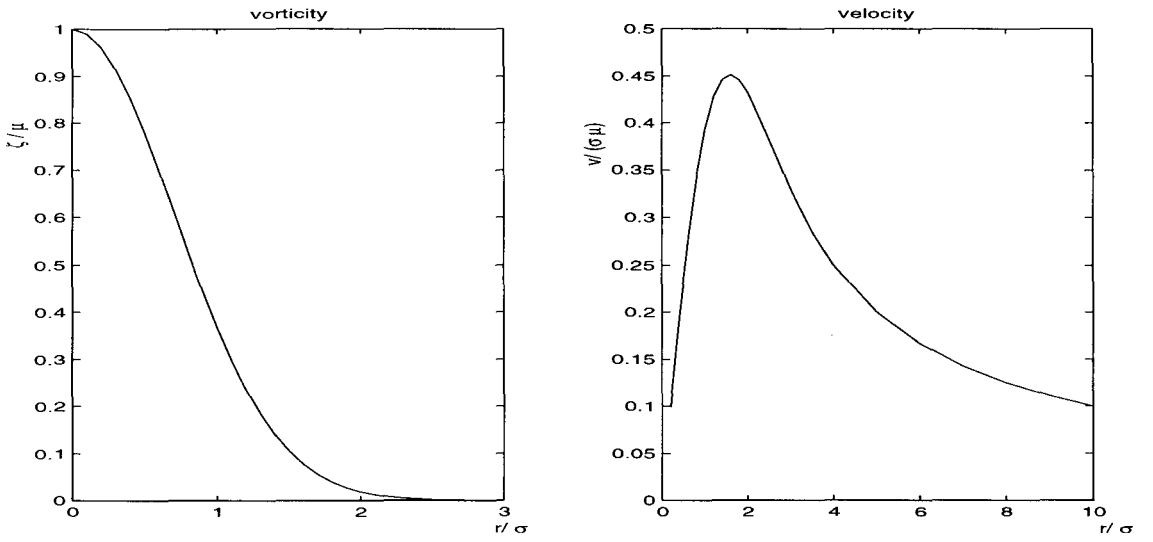


Figure 3.2: *The vorticity (3.4) and the azimuthal velocity (3.3) profile of a sink vortex*

The initial (x,y)-position where the vortices are created is (110 *cm*, 35 *cm*). See figure 3.1 for the coordinate mapping.

Some time after the vortex that has been created, it detaches from the initial position towards the north-west. This detachment takes less time when the water is more shallow. In table 3.2 it can be found how long it takes before the vortex starts to travel, at the different water depths. Just before the vortex detaches from the starting point, the syphoning of the water is stopped.

| Experiment | Water depth H (*cm*) | Syphoning time (*s*) |
|---|---|---|
| 1 | 12 | 30 |
| 2 | 18 | 45 |
| 3 | 24 | 60 |

Tabel 3.2: *Syphoning times for each experiment*

## 3.3 Ekman times

The Ekman time scale is a measure of the decay rate of vortices due to bottom friction and is defined as [7]:

$$T_E = \frac{2}{f\sqrt{E}} \tag{3.5}$$

Here, the Ekman number is given by

$$\sqrt{E} = \frac{1}{\overline{H}}\sqrt{\frac{2\nu}{f}} \tag{3.6}$$

where $\overline{H}$ is the average water depth, which is simply the average between the maximum depth and the minimum depth. The experiments were done for different maximum water depths: H=12, 18 and 24 *cm*. Since the minimum depth is always 8 cm less than the maximum depth (i.e. the slope of the bottom was kept constant) this results in average water depths of $\overline{H}$=8, 14 and 20 *cm*. The corresponding Ekman times then become $T_E$= 120, 200 and 280 *s*, respectively.

In order to measure bottom friction effects, the duration of the laboratory experiments was of order of the Ekman time scale, at least.

## 3.4 Data processing

Quantative measurements were obtained in the following way. The water surface is covered by a large number of bright particles, which are small round pieces of paper with a diameter of about 1 mm. The particles must have a specific weight close to that of water. In this way, their influence on the fluid motion is minimal and they will have approximately the same velocity as the fluid. The camera above the tank provides video images of the flow during the experiments, which are recorded on video tape with the VCR. The results are analysed by means of the DigImage system with which the particles are tracked and their velocities obtained. It is important that the particles are homogeneously spread, so they do not cluster together and they can still be independently tracked. Furthermore, it is important to have enough particles in the centre of the vortex, in order to provide sufficient information for measuring vorticity and velocity fields.

The DigImage system [9] is a program specifically developed for analysing flows on video images. First a reference coordinate system is defined with a reference video image of the domain, which is recorded before the experiment. With this reference coordinate system, the program can determine where the particles are located.

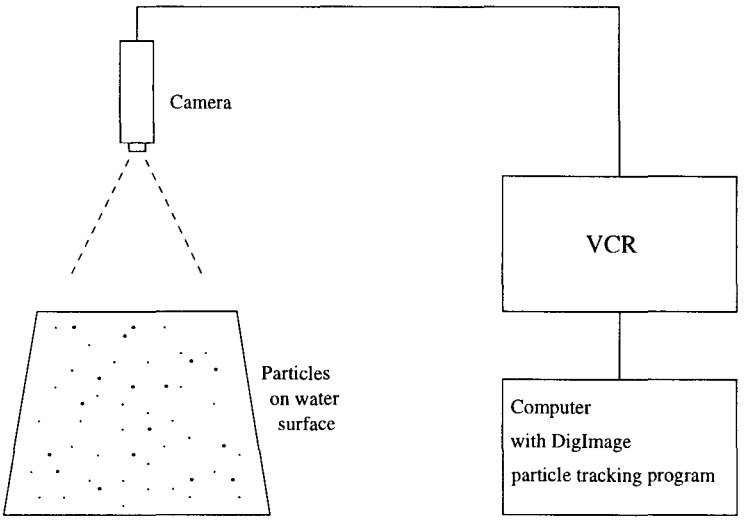


Figure 3.3: *Particle tracking the video images with the DigImage system*

Several thresholds, like the minimum and maximum brightness and the minimum and maximum size of the particles are prescribed in the program in order to determine whether a bright spot in a video image is a particle or not. The particles are identified in the next image (after time steps of 0.12 $s$) on their new position. In this way, the path of each particle is determined during the experiment. DigImage then calculates the corresponding velocities. Each experiment contains about 1000 to 1500 particles.

With the position and velocity data of the particles, velocity and vorticity fields are interpolated on a grid of 64x64, by means of an additional program called DGP. The interpolated velocity and vorticity fields are used to analyse the decay of the vortices. Further information on DigImage can be found in [9] and [10].

# Chapter 4

# Experimental results

In this chapter, the most important results showing the vortex decay on the sloping bottom are presented. First, the vorticity and the velocity profiles of a typical initial experimental vortex are shown. Afterwards, the decay of the peak vorticity at the vortex core and the vortex trajectories in experiments with different water depths is presented. Finally, some typical vorticity distributions are plotted.

## 4.1 Initial condition

In order to assess the initial characteristics of the vortices to be used on the topographic $\beta$-plane, the vorticity and velocity profiles of a vortex were determined immediately after being generated. These profiles are shown in figures 4.1 and 4.2. The radial coordinate $r$ is the distance from the grid points, in which the vorticity field is calculated, to the core of the vortex, which is at $r$=0.

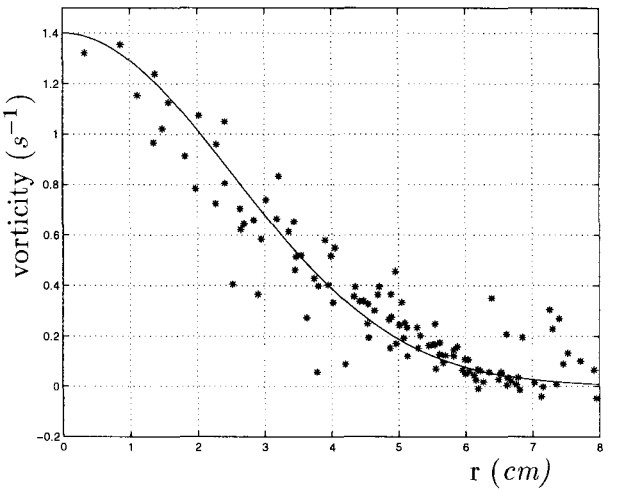


Figure 4.1: *The radial vorticity distribution of the vortex created in experiment 3 (H=24 cm) 30 seconds after the forcing was stopped, indicated by stars (*). The core of the vortex is at r=0. The solid line is a fit of equation (3.4) to the data. The parameters of the fit are* $\mu$=1.40 $s^{-1}$ *and* $\sigma$=3 *cm.*

Equation (3.4) was fitted to the data in figure 4.1 (compare with figure 3.2, left), by using a least squares method with $\mu$ and $\sigma$ as parameters. A least squares curve fitting is a method that minimizes the sum of the squared error at the data points [12]. The fit resulted in $\mu$=1.40 $s^{-1}$ and $\sigma$=3 $cm$ for this case.

Of all the data in figure 4.1, the maximum vorticity is 1.34 $s^{-1}$. Compared with the maximum vorticity according to the fit, $\mu$=1.40 $s^{-1}$, the difference is about 5 %. This comparison was also made for other vortices, and the difference between the measured peak vorticity and the fitting parameter $\mu$ was around 5 % in all the considered cases. Therefore it can be said that the maximum vorticity of the data points gives a good indication of the peak vorticity of the vortex.

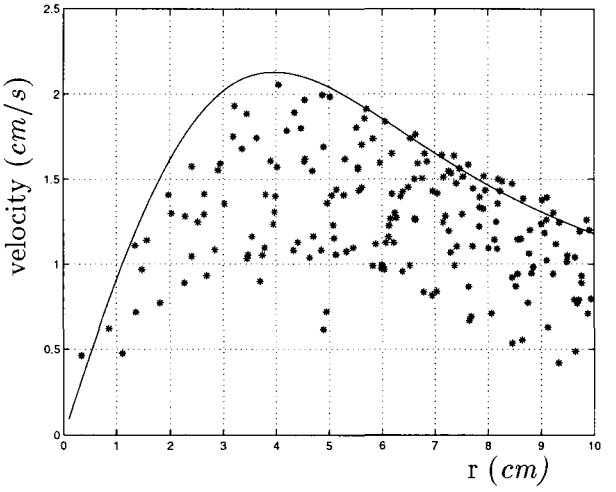


Figure 4.2: *The velocity profile of the vortex measured in experiment 3 (H=24 cm) after 30 seconds, indicated by stars (*). The core of the vortex is at r=0. The solid line is equation (3.3) with the parameters $\mu$=1.40 $s^{-1}$ and $\sigma$=0.03 m, obtained from the fit in figure 4.1.*

In figure 4.2 the velocity profile of the same vortex is determined. The values for $\mu$ and $\sigma$ that were obtained from fitting equation (3.4) to the vorticity profile were inserted in equation (3.3), represented by the solid line in figure 4.2 (compare with figure 3.2, right).

As can be seen, most of the measured velocities are smaller than the obtained curve. The reason for this is that the vortex does not have a perfectly circular shape and therefore, the velocity profiles vary for different cross-sections. In figure 4.3 the velocity profiles measured in the four quadrants are shown. As can be observed, the velocities are larger in the upper quadrants. The reason for this asymmetry is the topographic $\beta$-plane. In quadrants 1 and 2 the water depth is smaller, which implies that the fluid columns are squeezed, giving rise to larger velocities.

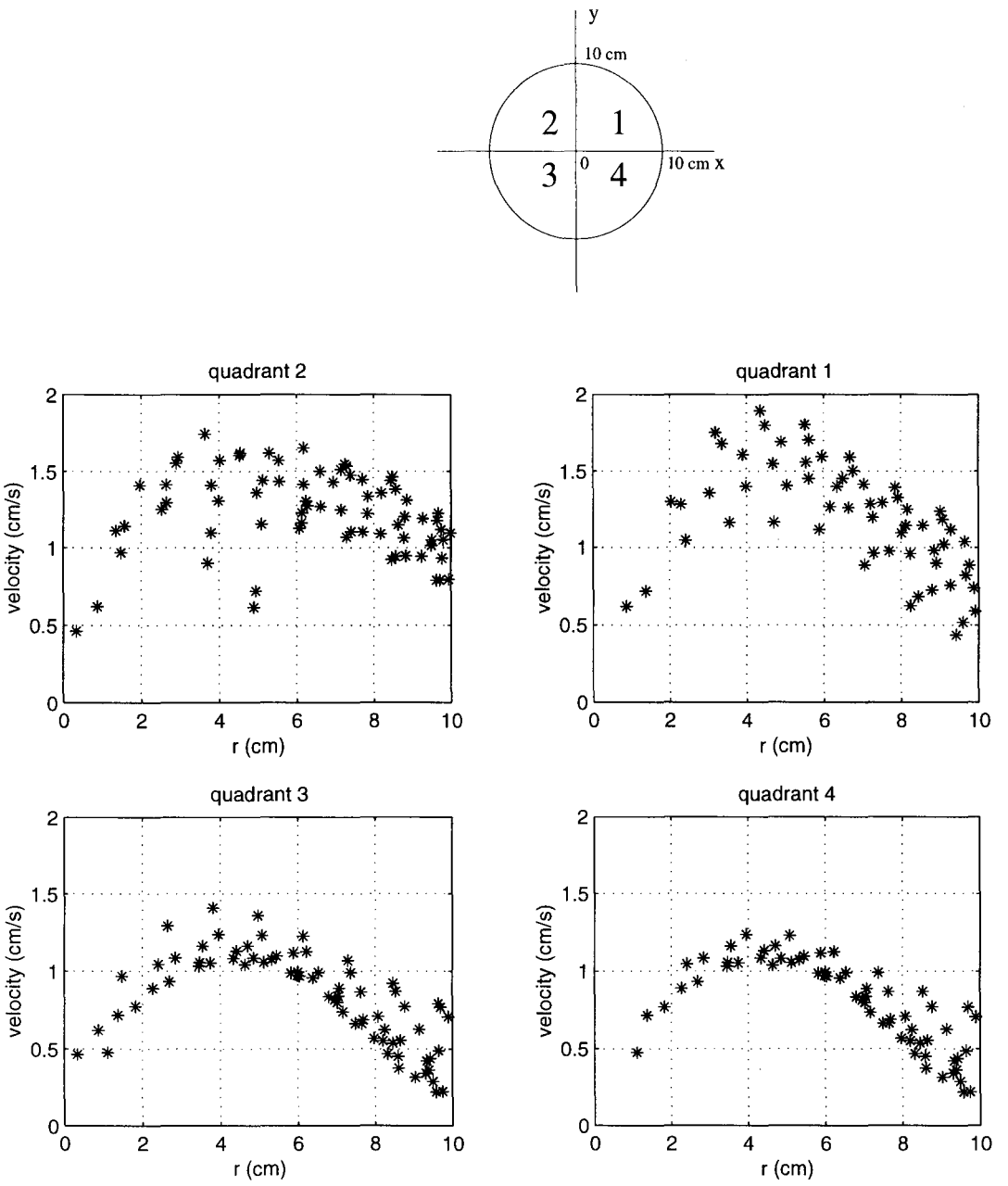


Figure 4.3: *The velocity profiles for the quadrants as indicated in the upper plot. Note that the lower quadrants, i.e. those with the larger water depths, have smaller velocities.*

## 4.2 Peak vorticity decay

During the course of some experiments, the peak vorticity of the vortex was determined until the vortex was no longer distinguishable from its surroundings, i.e. when the vortex has decayed almost completely. The results for the experiments with water depth H=24 *cm*, H=18 *cm* and H=12 *cm* are shown in figure 4.4, indicated by stars (∗). For all water depths the experiments were repeated several times. In all cases the vortices showed similar behaviour as the experiments shown here.

In [11] an equation is suggested for the peak vorticity decay of monopoles, including Ekman effects, for the case of a flat bottom:

$$\omega = \frac{\omega_0 e^{-t/T_E}}{\frac{\omega_0}{f}(1 - e^{-t/T_E}) + 1} \tag{4.1}$$

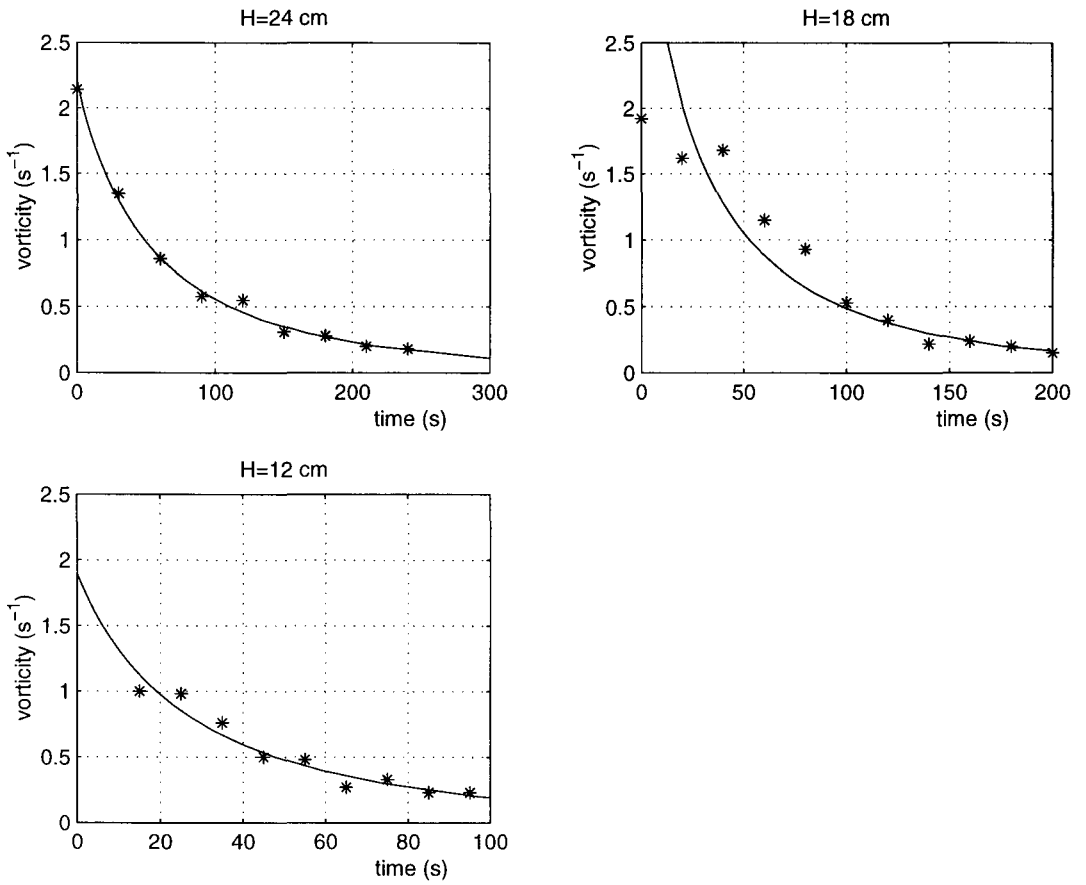


Figure 4.4: *The decay of the vortices, indicated by the stars (∗), measured by the peak vorticity. The solid line is a least squares fitting to equation (4.1). The time intervals are 30 s for H=24 cm, 20 s for H=18 cm and 10 s for H=12 cm.*

with $t$ the time, $\omega$ the peak vorticity of the vortex, $\omega_0$ the initial peak vorticity at $t = 0$, $T_E$ the Ekman time and $f$ the Coriolis parameter. This equation was fitted to the experimental data, using a least squares method with $\omega_0$ and $T_E$ as parameters. The results of the fittings are shown in figure 4.4, indicated by the solid lines. The calculated Ekman times and initial peak vorticities are shown in table 4.1. Here the theoretical values, calculated with equation (3.5), are compared with the fitted values.

Note that the first data points for experiment 2 (H = 18 *cm*) have a larger difference to the fitted curve than the other data points. The reason is that there were relatively few particles in the centre of the vortex at the beginning of this experiment. With fewer particles the determination of the peak vorticity is less accurate. Thus the error in the obtained result is larger than the errors estimated in section 4.1.

| | $T_E$ Theory | $T_E$ Fit to experiment | $\omega_0$ Fit to experiment |
|---|---|---|---|
| H = 24 cm | 280 s | 153 s | 2.19 $s^{-1}$ |
| H = 18 cm | 200 s | 115 s | 4.02 $s^{-1}$ |
| H = 12 cm | 120 s | 71 s | 1.89 $s^{-1}$ |

Table 4.1: *The Ekman times derived from fitting equation (4.1) to the experimental data compared with the theoretically calculated values.*

Comparing the Ekman times of the theory and the fit to the experiment, it can be seen that the value fitted to the experimental data is about 57 $\pm$ 2 % of the theoretical value in each experiment. This is a remarkably large difference. In the various experiments that were performed the difference remains. Thus, the decay rate of a monopolar vortex on a $\beta$-plane is essentially different from the decay on a flat bottom. The influence of a bottom topography is not included in definition (3.5), which shows to be not a good approximation for the Ekman time scale on a $\beta$-plane.

Large differences between the theory and the fit to the experiment were also found by [16] for unstable monopoles on a $\gamma$-plane. However, the fit was done with an exponential equation and not with equation (4.1). The experimental value found in that study was 52 % of the theoretical value. In [17] a better agreement between the experimental and the theoretical value was found. In this case experiments were performed with axisymmetric stable vortices on a flat bottom. The fit was also done with an exponential equation. In this case the ratio between the experimental value and the theoretical value was 83 %.

## 4.3 Vortex trajectories

Trajectories of the vortices were derived from the video images of the experiments. Using this method, the centre of the quasi-circular fluid motion is considered as the vortex position, which was determined each 10 seconds. The obtained results are shown in figure

4.5. Another way to determine the path of the vortex is by calculating the positions of the peak vorticity, which are considered as the centre of the vortex. The distance between the grid points is 1.4 *cm*, resulting in a maximum aberration of $\pm$ 0.7 *cm* for the vortex centre. The results of the method using the video images are within 5 % of the results of the method using the positions of the peak vorticity.

The direction of the path of the vortex is quite similar in the three experiments. However, the travelling time is different. In the first experiment, there is no longer any significant motion after about 220 to 240 seconds. In the second experiment, the motion stops at about 160 to 180 seconds, while in the third experiment the vortex desintegrates after about 60 to 80 seconds. This clearly indicates that bottom friction is more effective for lower depths.

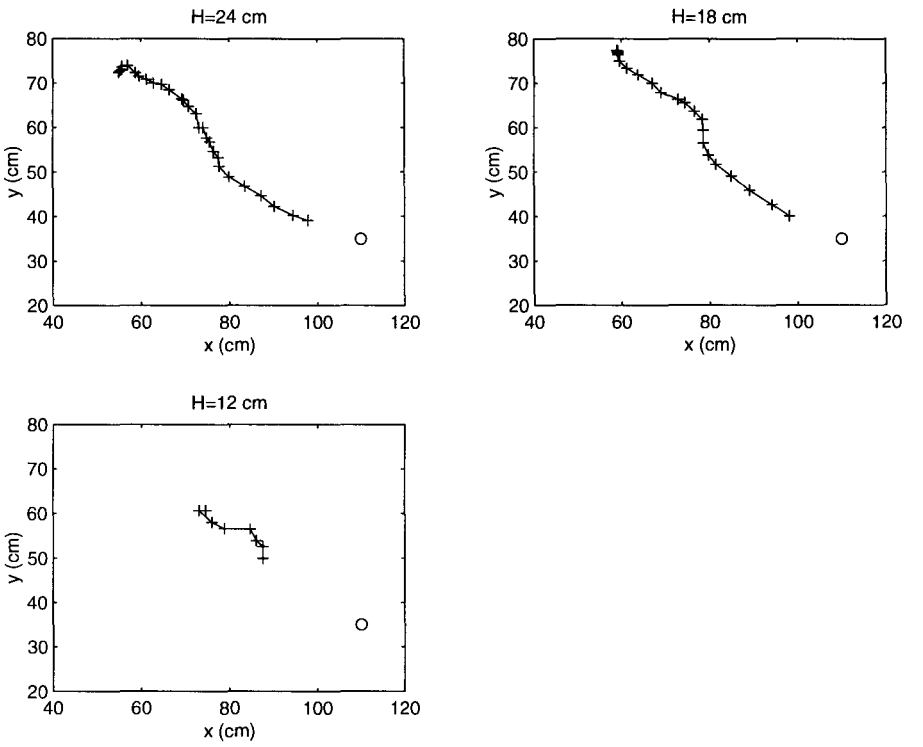


Figure 4.5: *The trajectories of the vortex in the different experiments. The circle indicates the position where the vortex was created. The time step between each measurement is 10 seconds. The motion is from the south-east to the north-west.*

## 4.4 Flow fields

Relative vorticity contours of each experiment are shown in figures 4.6 through 4.8. In these figures it can be seen how the vortex decays during its north-western drift. Note that at the end of each sequence the vortex is almost indistinghuisable from its surroundings. At these times the measurements were stopped.

The interval between two contours is 0.1 $s^{-1}$. This small value results in a lot of 'noise' far from the vortex. However, choosing this interval allows a view of the weak vorticity cells induced by the vortex.

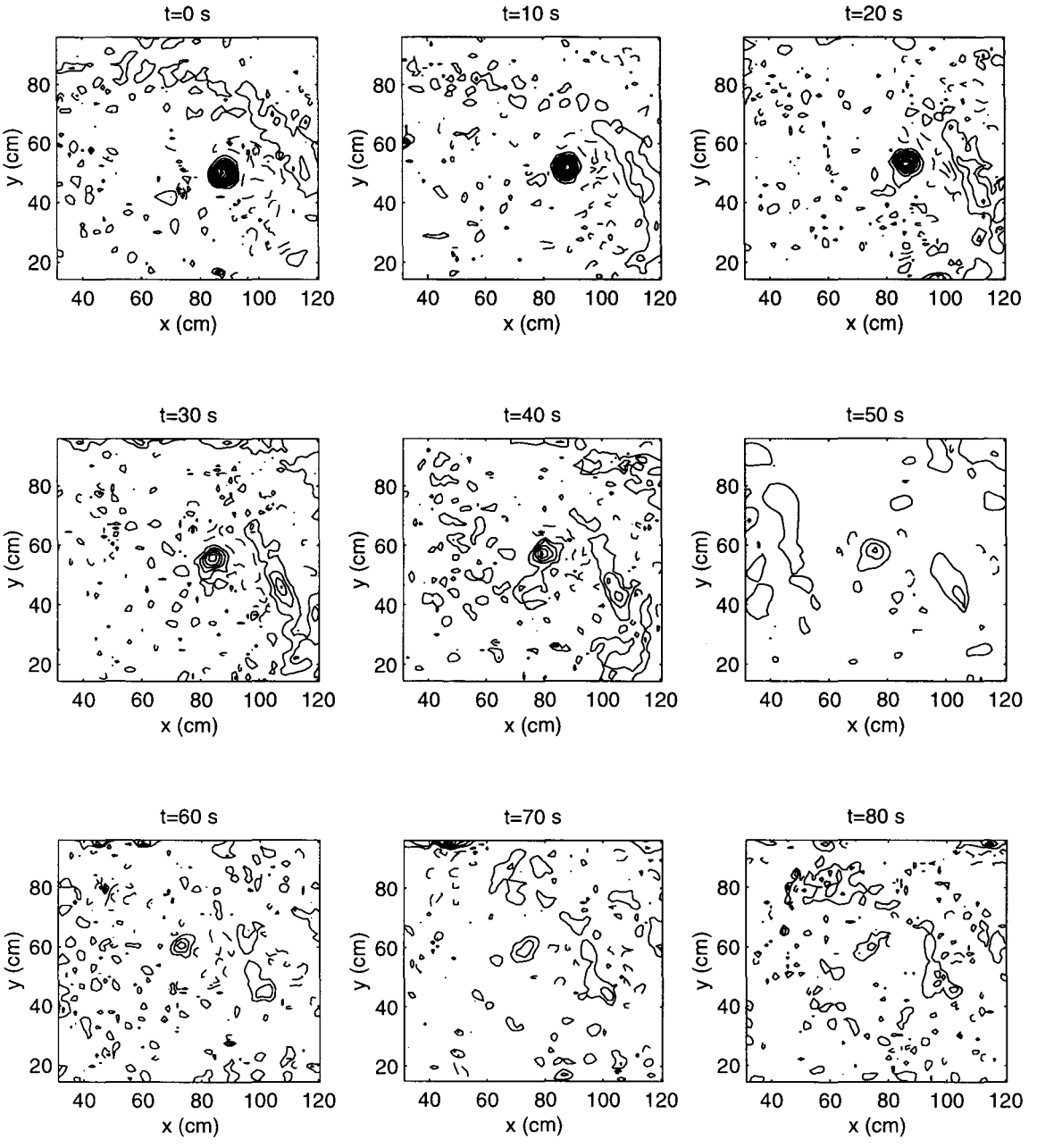


Figure 4.6: *Sequence of vorticity contours from experiment 1 (H=12 cm). The interval between two contours is 0.1 $s^{-1}$. The solid lines indicate positive vorticity and the dashed lines indicate negative vorticity.*

The creation of Rossby waves can be observed in these figures. In figure 4.6 a cell of negative vorticity arises at the north-east of the vortex. Further to the east, a patch of positive vorticity is also created, which is clearly seen at $t$=30 $s$. The centre of the negative cell is approximately at (95 $cm$, 55 $cm$) and the centre of the positive cell is approximately at (110 $cm$, 45 $cm$) Note that these cells are weaker than the vortex itself and therefore they also decay faster.

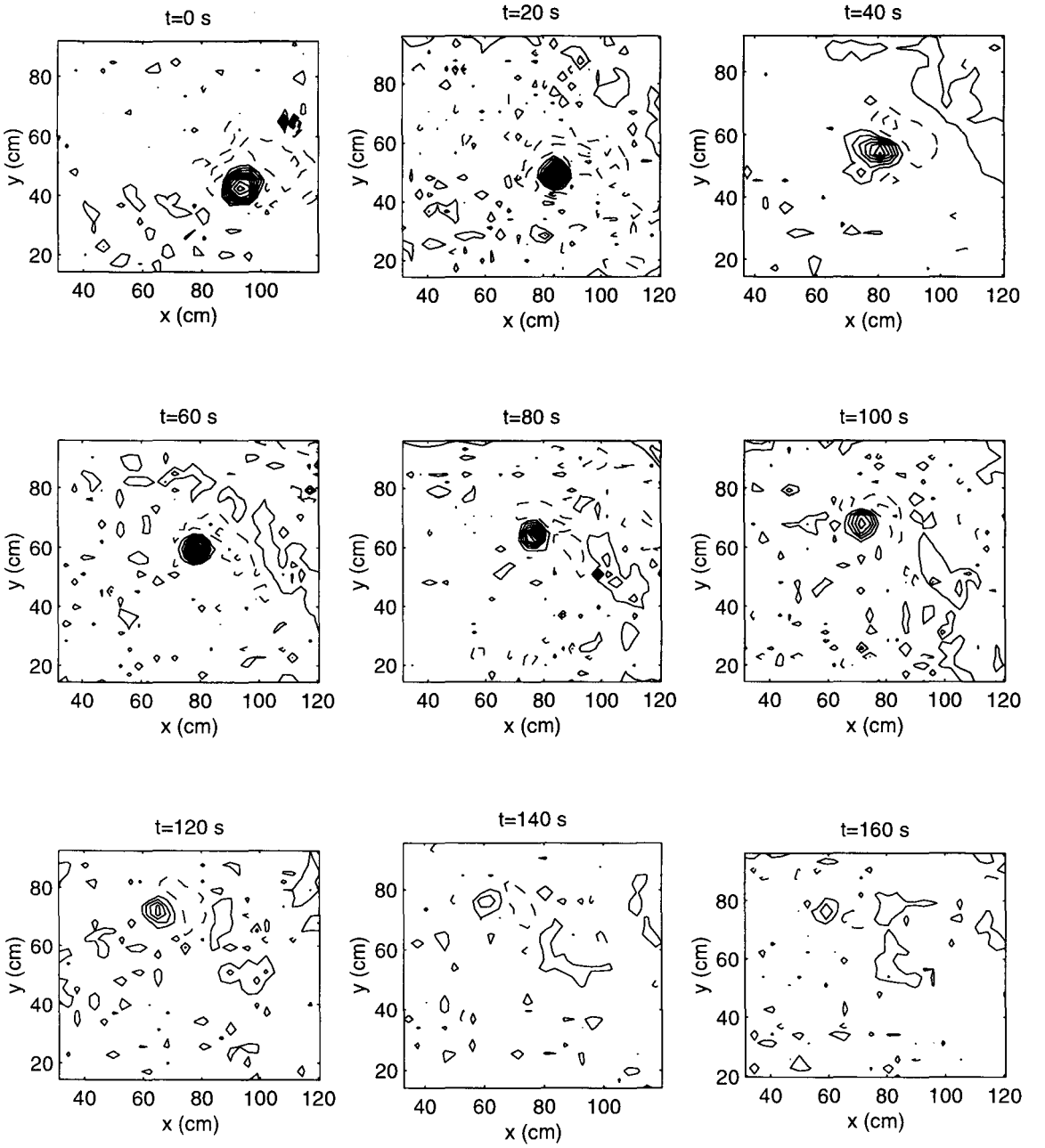


Figure 4.7: *Sequence of vorticity contours from experiment 2 (H=18 cm). The interval between two contours is 0.1 $s^{-1}$. The solid lines indicate positive vorticity and the dashed lines indicate negative vorticity.*

Figure 4.7 gives another example of the Rossby wave radiation. At $t$=40 $s$ a patch of negative vorticity can be distinguished to the north-east of the vortex. In the next time-frame, at $t$=60 $s$, a positive cell has also appeared, east of the negative vorticity patch. In the next frames it can clearly be seen, by looking at the positions of the vortex and the negative and positive cells behind it, that the Rossby wave travels to the west.

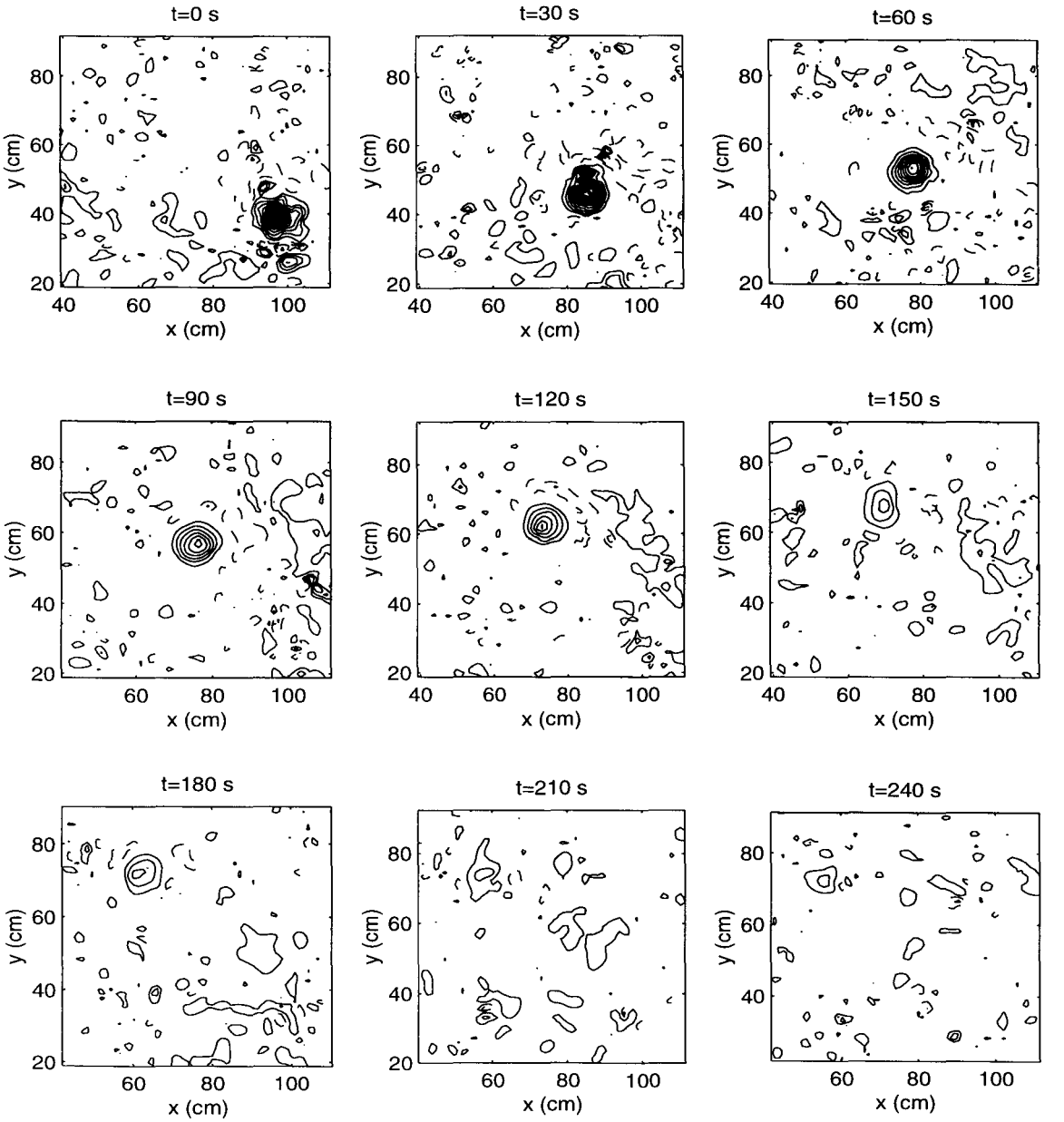


Figure 4.8: *Sequence of vorticity contours from experiment 3 (H=24 cm). The interval between two contours is 0.1 $s^{-1}$. The solid lines indicate positive vorticity and the dashed lines indicate negative vorticity.*

The positive vorticity induced at the south-west of the vortex (see figure 2.4) is very weak and contributes to the vortex distortion. However an example of such a cell can be seen in figure 4.7 at $t$=40 $s$. Similar results were obtained by [3].

In figure 4.8 the positions of the negative and positive cells can be distinguished best at $t$=120 $s$. Here the centre of the negative cell is approximately at (85 $cm$, 65 $cm$) and the centre of the positive cell is approximately at (100 $cm$, 60 $cm$). At $t$=0 $s$, the formation of the vortex has not been completed; therefore, the vortex is very asymmetrical. In the next frames the vortex acquires a more circular shape and becomes stable.

The velocity field of each experiment was also determined. These results can be found in appendix A (figures A.1 through A.3).

## 4.5 Dye experiments

Another way of visualising the vortex evolution is by using fluorescent dye. Just after the vortex is created the dye is injected in its core. In figure 4.9 the results of a typical dye experiment are shown for the case of H = 18 $cm$. The vortex was created at the second hole from below in the bar shown on the right side of the pictures, which is located at (110 $cm$, 35 $cm$), approximately.

In the first frame of figure 4.9 the vortex is still being created. As the vortex drifts to the north-west, it carries in its core all the injected dye. At $t$=120 $s$, however, some dyed fluid is released from the north-eastern part of the vortex to the ambient. The shedding of dyed fluid is caused by the squeezing of the vortex as it moves toward smaller water depths and by bottom friction.

The radius of the circle in which the dye was injected was approximately 7 $cm$. For larger radii, the release of fluid to the ambient is more clearly observed. This will be shown in the numerical simulations of next chapter, where passive tracers are initially put in a larger circle.

A typical example of a dye experiment with a monopolar vortex on a topographic $\beta$-plane can be found in [3]. In that case, however, a so-called stirring vortex [2] was used instead of a sink vortex.

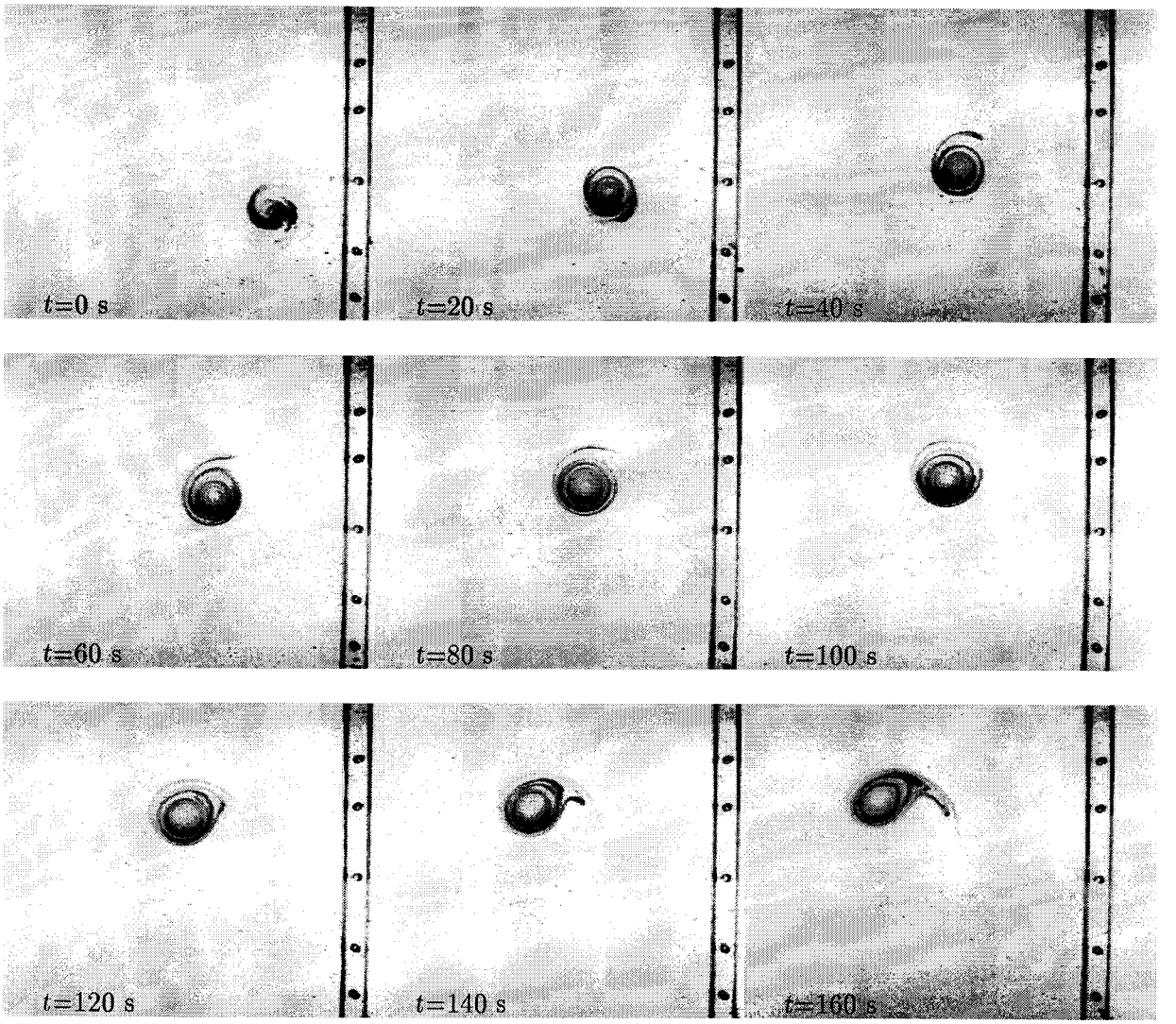


Figure 4.9: *Sequence of dye experiments for $H = 18$ cm. The starting point of the vortex is at the second hole from below in the bar at the right side of the pictures.*

# Chapter 5

# Numerical simulations

## 5.1 The numerical code

With the software package NSEVOL [6] several numerical simulations were performed. The program NSEVOL solves the modified two-dimensional Navier-Stokes equations in the vorticity-streamfunction formulation, given by models 1 through 4 (see table 2.1). The code computes the evolution of a certain initial vorticity distribution. The simulations were done at different water depths, with and without bottom friction and with and without variable topography.

The simulations were performed with initial conditions that approximate the laboratory conditions as good as possible. In all cases the initial vorticity distribution was given by equation (3.4), which represents a sink vortex. The time step of each new calculation was 0.1 $s$, and the result was written to an output file every 10 seconds. The numerical code uses a finite difference method [6]. This means that the vorticity equation is solved on a rectangular grid, which consisted of 129 $\times$ 129 points for each simulation. The domain was chosen the same as the rotating tank in the laboratory experiments: 150 $\times$ 100 $cm$. The initial position of each simulated vortex was the same as the experimental initial position, i.e. $(x_0, y_0) = (110\ cm, 35\ cm)$.

In each simulation the motion of passive tracers was also calculated. One tracer was put in the centre of the vortex in order to track its trajectory. Furthermore, 100 tracers were randomly put within the initially circular vortex. These tracers were followed in order to examine how the vortex was deformed and to make a qualitative comparison with the dye experiment presented in the last chapter.

The goal of the first simulations (section 5.2) was to approximate the results of the laboratory experiments. The strength of the vortices and their length scales were varied in order to obtain the best comparison. These values can be found at each individual simulation. The subsequent simulations, based on different 2D-models, were performed to examine the influence of the bottom friction (section 5.3) and the linear bottom topography (section 5.4).

## 5.2 Comparison with experiments

First, simulations were done based on the 2D model with bottom friction and variable topography given by equations (2.46) and (2.47). A topographic $\beta$-plane was prescribed for the depth field. The goal of these simulations was to approximate the results of the laboratory experiments with three different water depths. In table 5.1 the initial peak vorticities and length scales of the vortices are shown:

| | $\omega_0$ | R |
|---|---|---|
| H = 12 cm | 1.77 | 0.03 |
| H = 18 cm | 1.99 | 0.04 |
| H = 24 cm | 1.27 | 0.05 |

Table 5.1: *The initial vortex parameters $\omega_0$ and R*

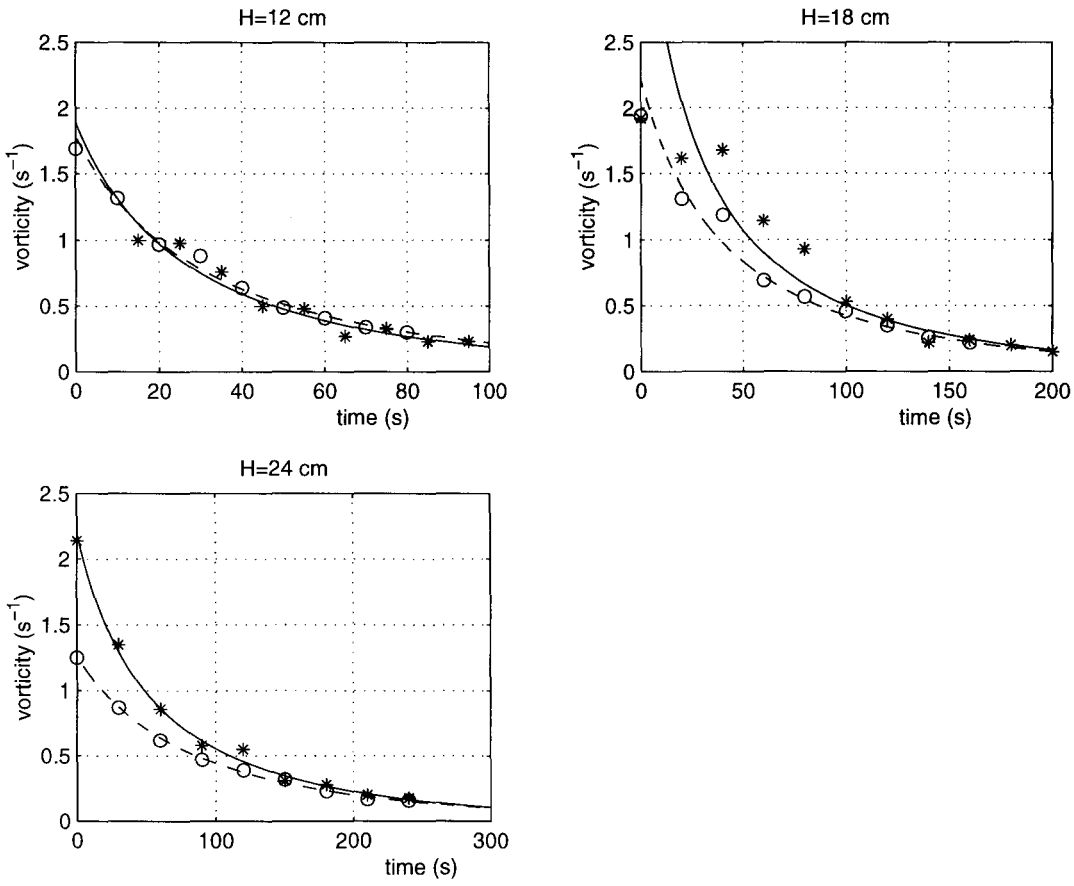


Figure 5.1: *The decay of the vortex in the numerical simulation compared with the decay in the experiment. The solid curve is fitted on the experimental data (∗) and the dashed curve is fitted on the simulation data (o)*

The vortex decay in these simulations was comparable to the decay in the experiments (see figure 5.1). Equation (4.1) was fitted to the results, using the same procedure as in section 4.2. The decay profiles of both the experiments and the simulations are also shown in figure 5.1. Finally, the Ekman times calculated from the simulations, according to equation (4.1), are shown in table 5.2, where they are compared to the Ekman times calculated from the experimental data.

| | $T_E$ Fit to experiment | $T_E$ Fit to simulation |
|---|---|---|
| H = 12 cm | 71 s | 76 s |
| H = 18 cm | 115 s | 120 s |
| H = 24 cm | 153 s | 167 s |

Table 5.2: *Comparison of the Ekman times of the simulations and the experiments. The Ekman times were derived from fitting equation (4.1) to the data.*

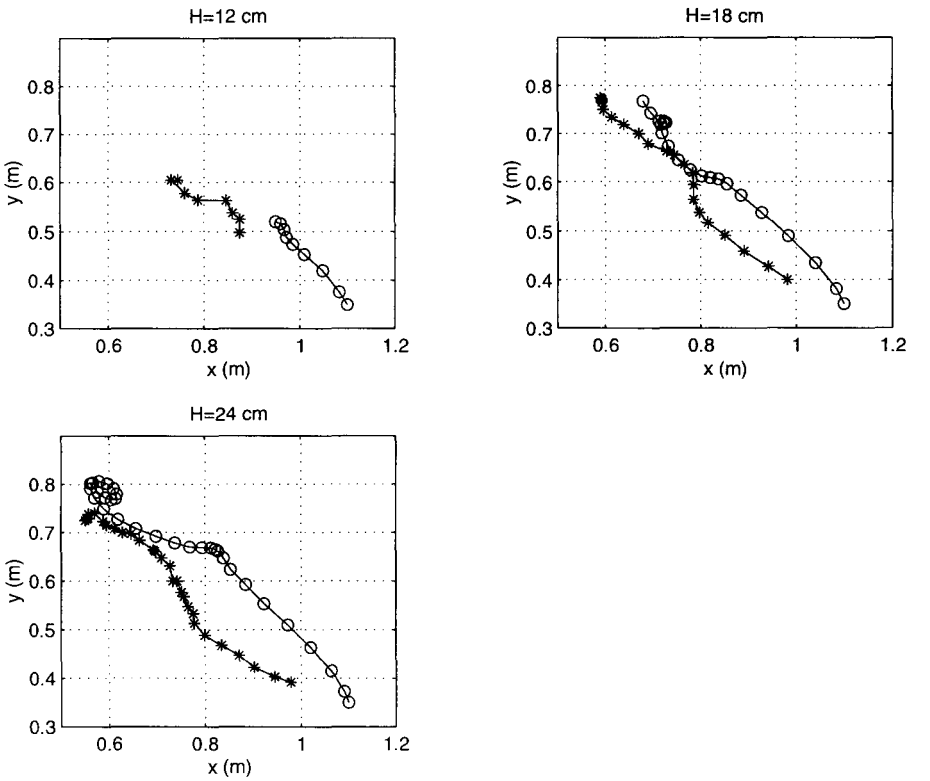


Figure 5.2: *The trajectories of the vortices in the experiments compared with the vortices in the simulations; Trajectories indicated with stars (∗) are the experiments and trajectories indicated with circles (o) are the simulations (without friction). The position was determined every 10 seconds.*

In figure 5.2 the vortex trajectories in the simulations are compared with those in the experiments. The trajectory was determined by means of the peak vorticity position in time-steps of 10 seconds. It can clearly be seen that the vortices of the simulations stop moving after a similar time-scale as in the experiments. These time-scales are shown in table 5.3. Furthermore, both the experimental and simulated vortices move in the same direction. A difference between their trajectories is the starting point. In both cases the vortex starts at (110 *cm*, 35 *cm*); however, the experimental vortex takes some time (about 30 to 60 seconds, see table 3.2) before it is created, while the simulated vortex is formed instantaneously. During this time the experimental vortex starts to drift due to the influence of the topographic $\beta$-plane. Thus, before the measurements can start, the vortex has already drifted away several centimeters.

| | experiment | simulation |
|---|---|---|
| H = 12 cm | 70 $\pm$ 10 s | 70 $\pm$10 s |
| H = 18 cm | 170 $\pm$ 10 s | 160 $\pm$ 10 s |
| H = 24 cm | 230 $\pm$ 10 s | 220 $\pm$ 10 s |

Table 5.3: *The estimated times at which the vortices stop moving. These values are similar for the experiments and the simulations.*

Plots of the temporal evolution of 100 tracers that were randomly put inside the initially circular vortex core were made. In figure 5.3 the result for H=18 *cm* is presented. The plots for the other water depths can be found in Appendix A (figures A.4 and A.5). Figure 5.3 shows that some of the tracers are leaking out of the (core of the) vortex from its north-eastern side. This effect was also present in the dye experiments (see figure 4.9), where the vortex released fluid to the ambient. A difference between the experiment and the simulation is the time at which the leaking of dye or tracers begins. This can be explained by the fact that the radius of the circle where the dye or tracers were put is different. For the tracers this radius was 10 *cm* and for the dye it was approximately 7 *cm*.

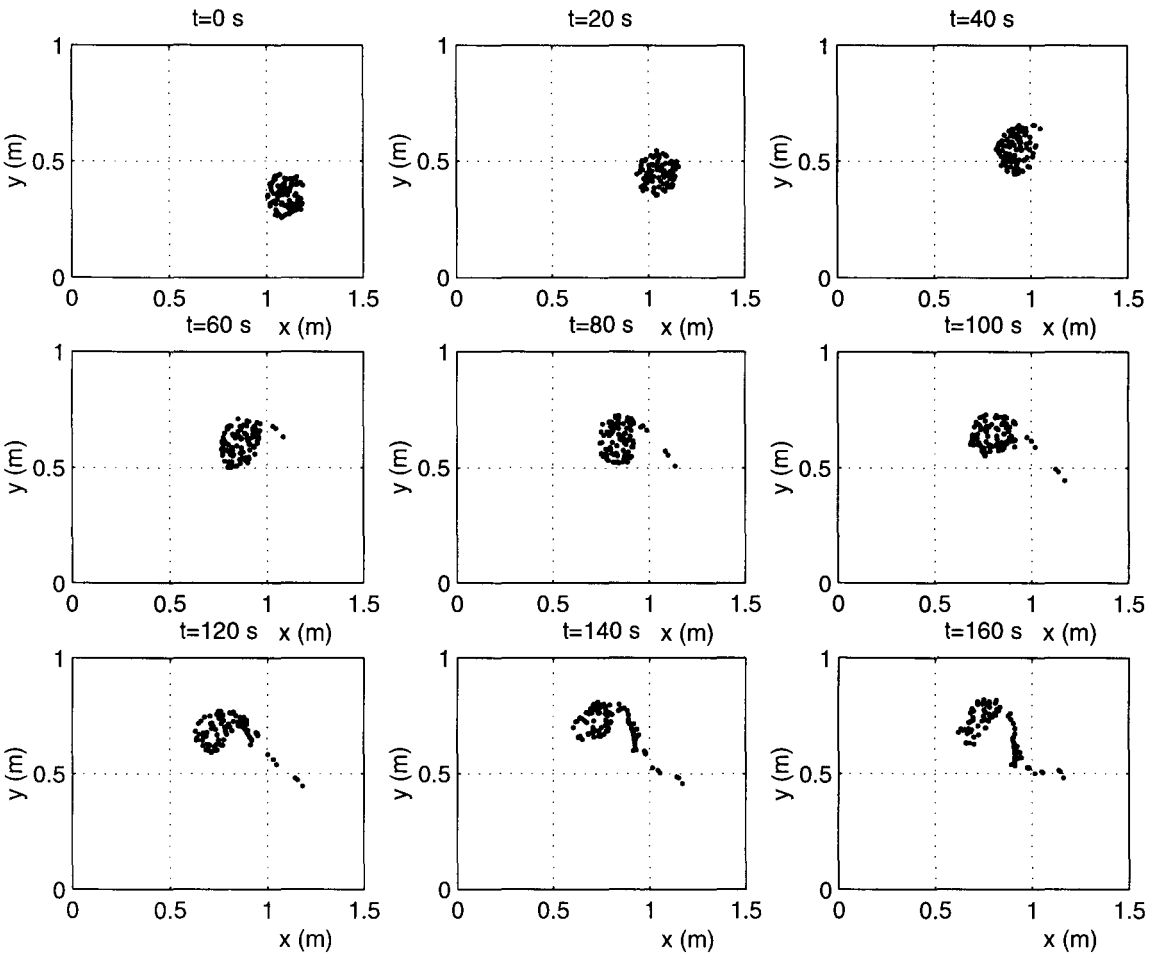


Figure 5.3: *Sequence of tracer positions for the simulation on a $\beta$-plane, including bottom friction due to Ekman layers, for the case of H=18 cm. 100 tracers were randomly put in a circle with radius 10 cm centred in the vortex core.*

Figure 5.4 shows the vorticity contours of the simulation with $H = 18\ cm$. Plots of the vorticity fields for other water depths can be found in appendix A (figures A.6 and A.7).

At the beginning of the simulation, the creation of positive and negative relative vorticity due to the $\beta$-plane is clearly observed. At $t$=20 $s$ a positive induced cell south-west of the vortex can clearly be distinguished, while a patch of negative vorticity is formed to the north-east. This initial stage of motion can be compared with figure 2.4, where the basic mechanism for the north-western drift of the vortex was shown. Later, the formation of Rossby waves can be clearly seen: after the induced cell with negative vorticity appears east of the vortex, a second induced cell with positive vorticity is developed ($t$=60 $s$). Compare this with figure 4.8. At $t$=120 $s$ even a third induced cell with negative vorticity can be seen, although it is very weak.

This simulation also shows the creation of vorticity at the no-slip walls.

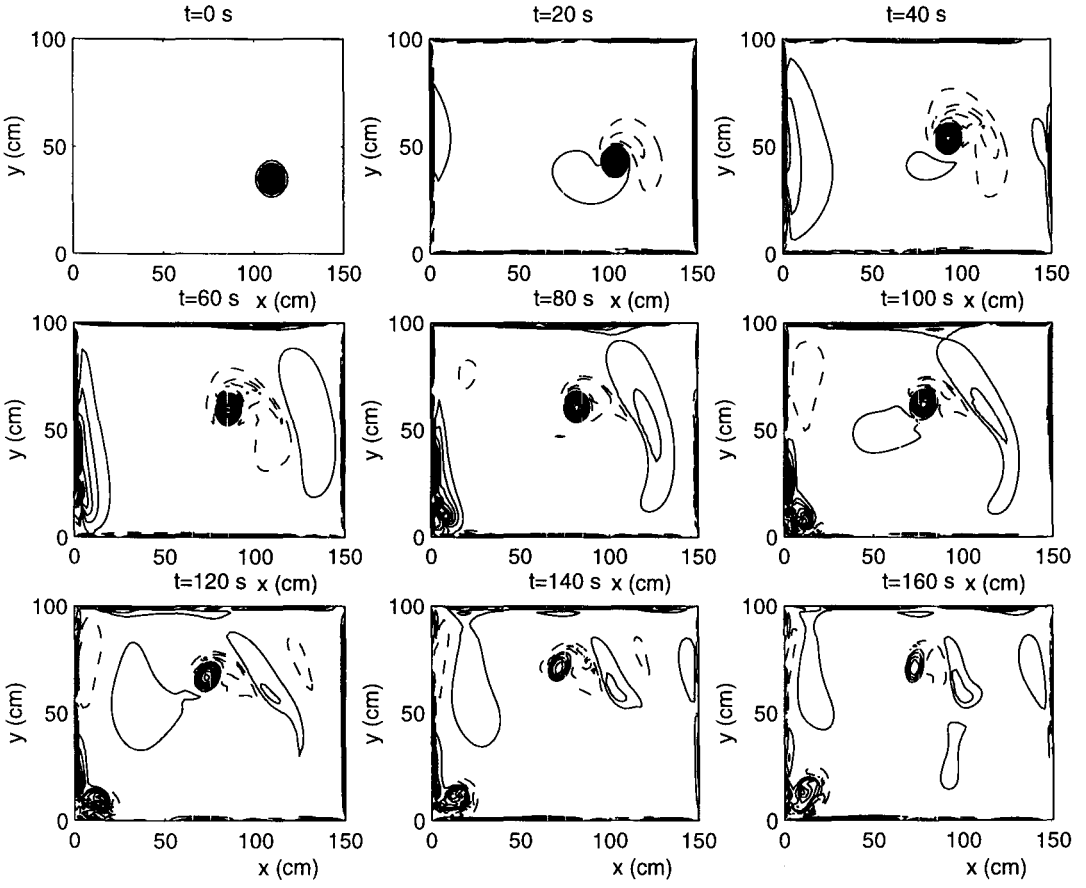


Figure 5.4: *Sequence of vorticity contours from the simulation on a β-plane, including bottom friction due to Ekman layers, for the case of H=18 cm. The interval between the contours is 0.05 $s^{-1}$. The solid lines indicate positive vorticity and the dashed lines indicate negative vorticity.*

## 5.3 Simulations without bottom friction

The simulations were repeated with the same initial conditions without including bottom friction, i.e. now the simulations are based on equations (2.43) and (2.45).

Again the peak vorticities were determined. The results are shown in figure 5.5, where they are compared with simulations including Ekman friction. As expected, the vortices that experience the influence of bottom friction decay faster than the vortices without bottom friction. The decay is now better described by:

$$\omega = \omega_0 e^{-t/T} \tag{5.1}$$

with T a characteristic decay time. The calculated peak vorticities are fitted to equation (5.1) for the simulation without friction and to equation (4.1) for the simulation with friction. A comparison of the values for T with those of $T_E$ can be found in table 5.4:

| | $T_E$ with bottom friction | $T$ without bottom friction |
|---|---|---|
| H = 12 cm | 76 s | 128 s |
| H = 18 cm | 120 s | 196 s |
| H = 24 cm | 167 s | 294 s |

Table 5.4: *The characteristic time T derived from fitting equation (5.1) to the data of the simulation without bottom friction and the Ekman time $T_E$ derived from fitting equation (4.1) to the data of the simulation including bottom friction.*

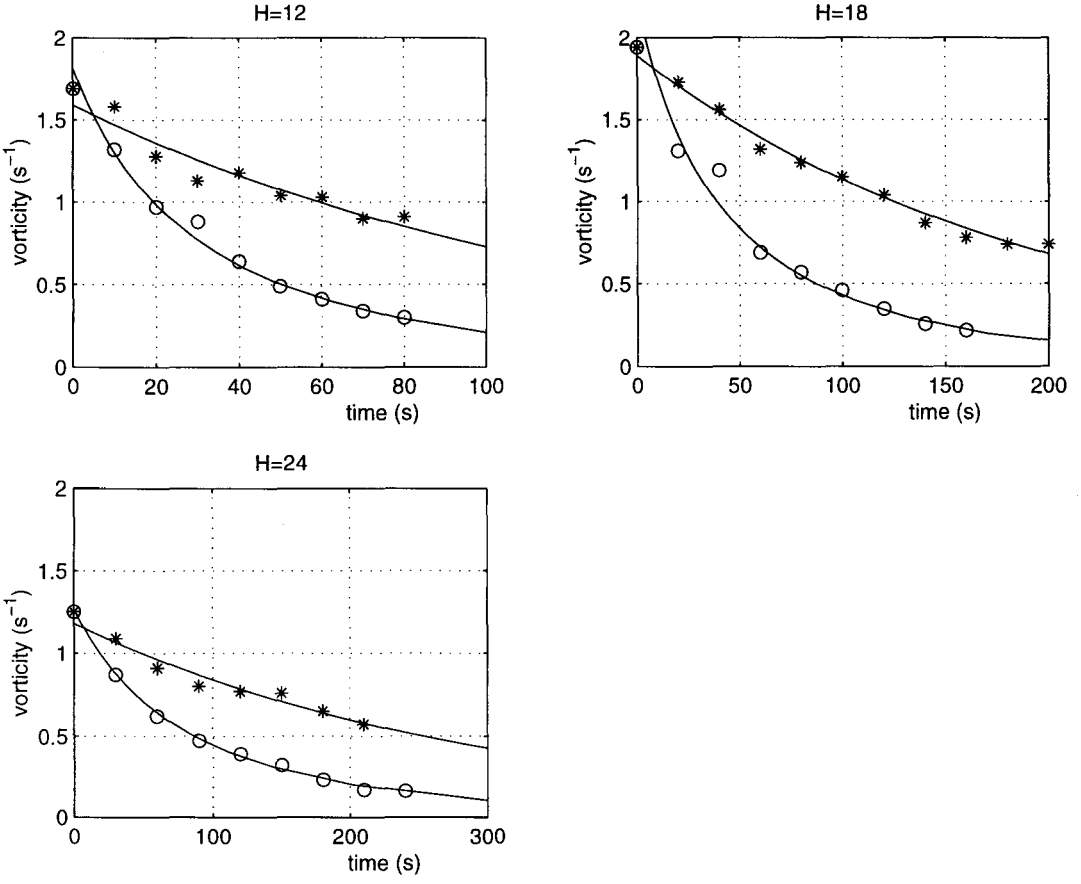


Figure 5.5: *The decay of the vortex in simulations without friction (∗) and in simulations with friction (o). The curves are fitted to equation (5.1) for the situation without friction and to equation (4.1) for the situation with friction.*

In figure 5.6 the trajectories of the simulations with and without friction are also compared. The position of the vortex was determined each 10 seconds. The influence of the bottom friction, manifested by the slower drift of the vortex, can be observed after 20 to 40 seconds. In simulations without bottom friction, the vortices move faster than in simulations including Ekman effects. At the beginning, however, their trajectories are similar.

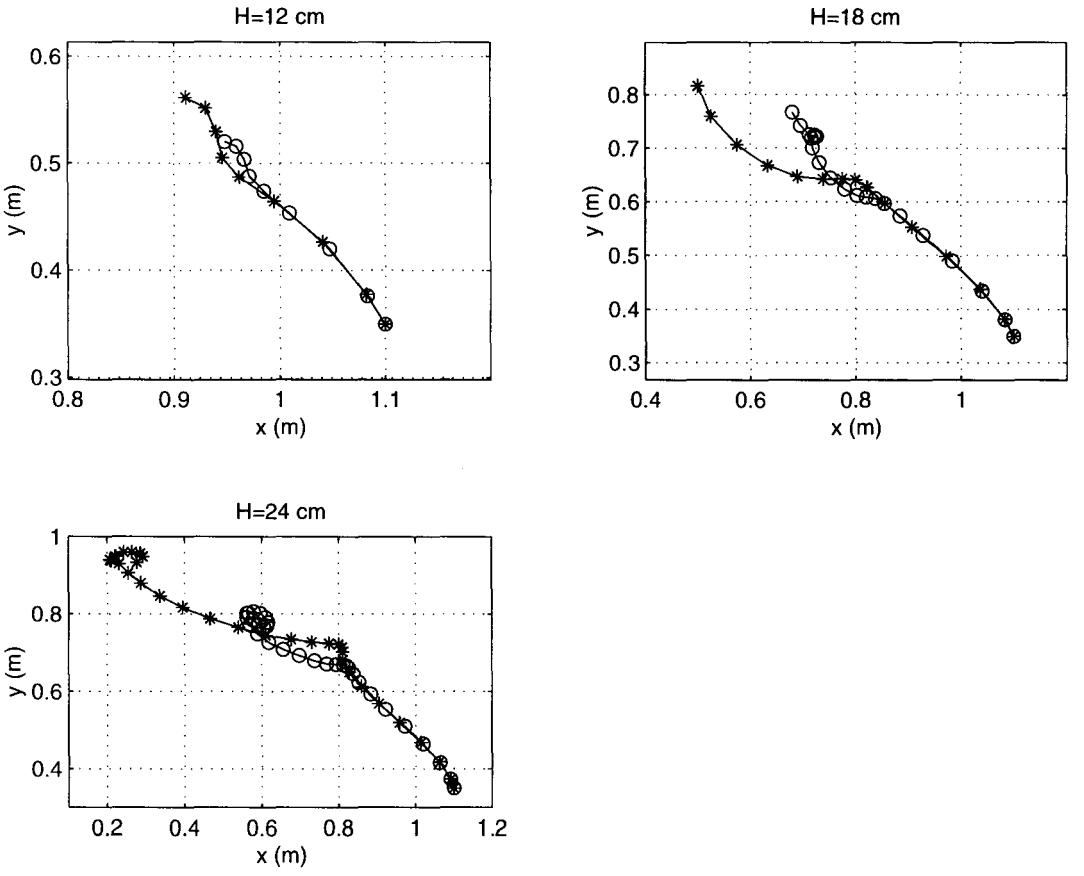


Figure 5.6: *The trajectories of the vortices in simulations with and without bottom friction. Trajectories indicated with stars (o) are from the simulations with friction and trajectories indicated with circles (∗) are from the simulations without friction. The position of the vortices was determined each 10 seconds.*

The plots of the vorticity fields can be found in appendix A (figures A.8 through A.10).

## 5.4 Simulations with flat bottom

Additional simulations were done by using a flat bottom and including bottom friction. The peak vorticity decay of the vortices on the flat topography is compared with the decay on a $\beta$-plane, as shown in figure 5.7. As can be seen, the vortices on the flat bottom have a slower decay rate than the vortices on the $\beta$-plane. The decay was fitted to equation (4.1), as was done similarly in [4], where it was found to be a good fit to represent the results. In table 5.5 the Ekman times of cases with and without the $\beta$-plane are compared:

| | $T_E$ $\beta$-plane | $T_E$ flat bottom |
|---|---|---|
| H = 12 cm | 76 s | 145 s |
| H = 18 cm | 120 s | 222 s |
| H = 24 cm | 167 s | 286 s |

Table 5.5: *The Ekman times for the decay on a flat bottom compared with the decay on a $\beta$-plane*

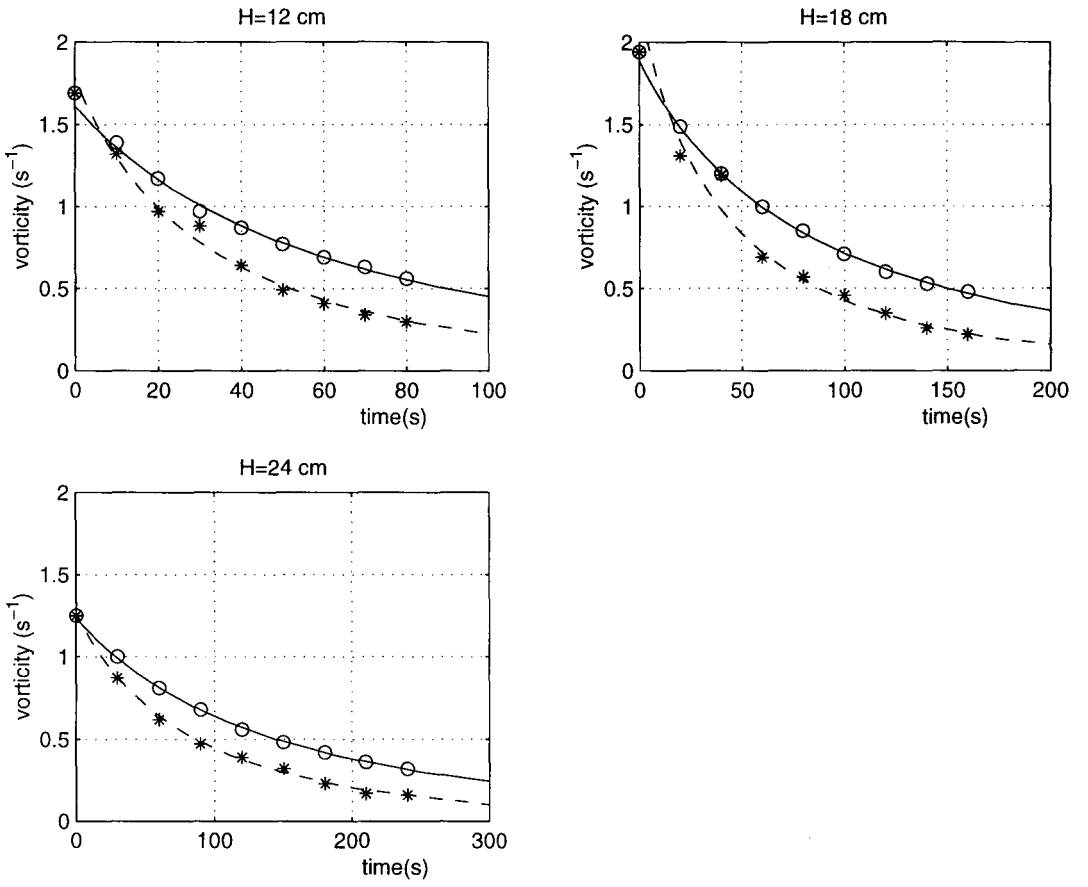


Figure 5.7: *The decay of the vortices on a $\beta$-plane, indicated with stars ($*$) compared with the decay on a flat bottom, indicated by circles ($o$). Both cases include bottom friction.*

The Ekman times of the vortices on the $\beta$-plane are $55 \pm 3$ % of the Ekman times on the flat bottom.

In the flat bottom case, the vortex remains at a fixed position and preserves its circular shape. This is because there are no changes in relative vorticity associated with depth variations (i.e. the water depth $H$ remains constant) that influence the vortex.

# Chapter 6

# Discussion and conclusions

In this study the evolution and decay of a non-isolated monopolar vortex on a topographic $\beta$-plane has been examined by means of laboratory experiments and numerical simulations. The topographic $\beta$-plane consists of a linear sloping bottom on which the vortex drifts to the north-west, while gradually decaying. This decay is associated with bottom friction (Ekman effects) and with Rossby wave radiation, due to the $\beta$-effect. The results are mainly focused on the vortex decay due to Ekman friction. These effects have been studied by using different water depths in the experiments and by performing numerical simulations (based on two-dimensional physical models) with or without Ekman friction.

The vortex evolution has been characterised by measuring the peak vorticity at the vortex core and by the north-western trajectory. Three representative experiments with different water depths (H=12, 18 and 24 $cm$) were chosen to show the main results. It was found that the lower the water depth the faster the vortex decay. This important result is mainly attributed to bottom friction effects, which are more effective for shallower depths. In fact, the decay rate associated with the no-slip bottom is usually measured by the Ekman time scale $T_E$ (see section 3.3), which is proportional to the depth. For times of order $T_E$, bottom friction effects become manifested.

In section 5.2 it was shown that the vortices decay in the experiments could be simulated with numerical runs based on the physical model given by (2.46) and (2.47). In the corresponding numerical simulations the Ekman times, calculated according to equation (4.1), were similar to those determined in the experiments. The trajectories of the vortices were also similar for the experimental and the numerically simulated cases, although the correspondence is not exact. This was due to the unavoidable differences between experimental and numerical initial conditions. The results, however, strongly suggest that the model of equations (2.46) and (2.47) is able to describe correctly the influence of bottom friction on the topographic $\beta$-plane.

One of the main results is that equation (4.1) gives a good description of the peak vorticity decay on the topographic $\beta$-plane. Equation (4.1) was derived before [4, 11] for the decay of monopolar vortices on a flat bottom. This was done by neglecting the non-linear terms and the viscous effects in equation (2.46). The differential equation then yields:

$$\frac{\partial \zeta}{\partial t} = -\frac{d_E}{2H}\zeta(\zeta + f) \tag{6.1}$$

For the flat bottom case (i.e. $H = H_0$) the factor $d_E/H_0$ is equivalent to $E^{1/2}$ (see section 2.5) and the solution is equation (4.1). Since this expression is valid for the topographic $\beta$-plane as well, the water depth $H(y)$ on the topographic $\beta$-plane can apparently be approximated by the average water depth $\overline{H_0}$. This depth can be calculated as the average between the water depth at the vortex core at the beginning and at the end of its north-western trajectory. In the present experiments the average depth in the rotating tank can also be taken.

The influence of the topographic $\beta$-plane was examined by comparing with simulations on a flat bottom. The Ekman times in the case of the topographic $\beta$-plane are about 55 % of the Ekman times in case of the flat bottom. There are two reasons for this considerably faster decay on the topographic $\beta$-plane compared with the decay on a flat bottom. One reason is the loss of energy due to the creation of Rossby-waves, shown in the vorticity contour plots (figures 4.6 through 4.8). Patches of negative and positive vorticity eastward of the vortex could clearly be distinguished in these plots. The second reason is the squeezing of the vortex as it drifts to the north. Because the viscous effects are small, the potential vorticity (equation (2.17)) is nearly conserved per fluid column. This results in decreasing vorticity in case of decreasing water depths.

In order to examine the influence of the bottom friction due to the Ekman layer, additional simulations were done in which this friction was not included. The decay in this case was best described with equation (5.1) and shows to be considerably slower. This implies that the bottom friction due to the Ekman layer plays a very important role in the decay of the vortex. This was already shown in [5] as well.

In table 6.1 the Ekman times of the experiments and the simulations, calculated according to equation (4.1), are again shown in comparison with the theoretical values, calculated by equation (3.5):

| Waterdepth | Theory | Experiment | Simulation 1 | Simulation 2 |
|---|---|---|---|---|
| H = 12 cm | 120 s | 71 s | 76 s | 145 s |
| H = 18 cm | 200 s | 115 s | 120 s | 222 s |
| H = 24 cm | 280 s | 153 s | 167 s | 286 s |

Table 6.1: *The Ekman times of the experiments and the simulations compared with the theory (equation (3.5)). The first simulation is with bottom friction on a topographic $\beta$-plane, the second simulation is with bottom friction on a flat bottom. All values are calculated from fitting equation (4.1) to the data*

The values shown in table 6.1 are plotted in figure 6.1. As can be seen, the Ekman times calculated from the theory give a good approximation for the case of a flat bottom when

bottom friction is included. For the case of a topographic $\beta$-plane, in contrast, the Ekman times drop to roughly half the values (compared with the flat bottom case).

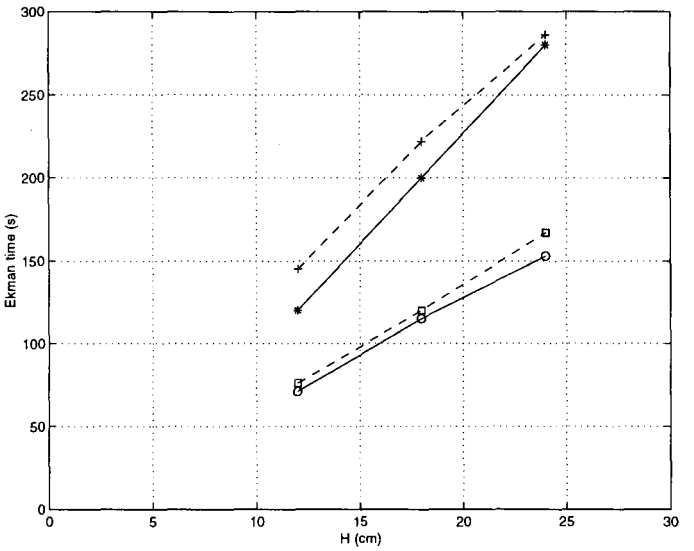


Figure 6.1: *Ekman times vs. water depth from Table 6.1. The upper part shows the theoretical values (stars, solid line) and the simulation with bottom friction on a flat bottom (pluses, dashed line). The lower part shows the simulation with bottom friction on the topographic $\beta$-plane (squares, dashed line) and the experiments (circles, solid line)*

These new values for the Ekman times on a topographic $\beta$-plane can be estimated as follows:

$$T_E(\text{new}) = aT_E(\text{theory}) = \frac{2a}{f\sqrt{E}} \tag{6.2}$$

with $a = 0.57 \pm 0.02$. This value is similar to the value found comparing the simulations on the flat bottom with the simulations on the topographic $\beta$-plane, as expected.

The shedding of fluid from the vortex core to the ambient was shown in figure 4.9, where a typical dye experiment was presented. This shedding of fluid can also be observed in the numerical simulations. In figure 5.3 passive tracers are released from the core of the vortex to the ambient, as the vortex drifts north-westward. The vortex leaks dye/tracers from its north-eastern part due to the squeezing of fluid columns as they move upslope in the cyclonic motion. This is a typical effect of translating vortices on a topographic $\beta$-plane, as shown by [3]. The curved trajectories of the vortices can be partially explained by this effect since the released fluid contains vorticity, which eventually affects the vortex motion. Note that a difference between the experiment and the simulation is the radius of the circle in which the dye or the tracers were initially put (about 7 *cm* in the experiments and 10 *cm* in the simulations). This causes the difference in the plots showing the released fluid.

It should be noted that the Rossby number in the experiments is initially $O(1)$, while the use of a topographic $\beta$-plane has only been justified for small values [13]. However, since the experimental vortices decay rather fast to smaller Rossby numbers, this is not expected to have a significant effect on the validity of the results.

The vortex parameters were determined from the initial vortex structure, which revealed its asymmetrical shape due to the sloping bottom. Equation (3.4) was fitted to the experimental vortices in order to obtain the peak vorticity at the vortex core and its characteristic length scale. In each case the difference between the maximum vorticity of the data points and the peak vorticity derived from fitting equation (3.4) was about 5 %. Furthermore it can be said that equation (3.4) fits to the vorticity profiles of the vortices (see figure 4.1), while equation (3.3), however, does not fit to the velocity profiles very well, as can be seen in figure 4.2. This is because the vortex is not exactly circular. The velocity profiles were determined for different directions and an asymmetry was found between the southern and the northern side (see figure 4.3). This asymmetry is due to the topographic $\beta$-plane. In the smaller water depths (the northern side) the vortex fluid is squeezed, giving rise to larger velocities.

The trajectories of the vortices were obtained by using the peak vorticities as the centre of the vortex, or by using the video images from which the vortex position was determined. The results of both methods did not differ more than 5 % from each other. The directions of the trajectories were similar for the different water depths, but the travelling times were different, due to the different decay rates. In the cases of larger water depths, the vortex moved further.

In the simulations, only a bottom Ekman layer is included, but not a surface Ekman layer produced by air friction. However, in the laboratory case air friction is negligible compared to the friction due to the bottom Ekman layer. Furthermore, the parabolic curvature of the surface is not included. The difference in water depth due to the curvature of the surface is maximum 5 $mm$ between the centre and the side of the tank. This is rather small compared to the smallest average water depth of 8 $cm$ that was used. Therefore the curvature of the surface will not be very important.

A comparison with real oceanic cases remains difficult. For geophysical flows, different and more complicated phenomena (such as density stratifications, more complicated bottom topographies and oceanic currents) play an important role in the evolution of monopolar vortices. Here it has been illustrated how a sloping bottom enhances the vortex decay; this situation could be applied, for instance, to study oceanic vortices in the presence of a continental shelf.

Some recommendations for further work would include investigation of the evolution and decay of other types of monopoles (like the stirring vortex [2]) and of dipoles and tripoles on a topographic $\beta$-plane. Experiments with stronger vortices and larger water depths will show more information about the decay of vortices, but for these experiments a larger tank will be needed. In order to obtain more information about the influence of the topographic $\beta$-plane, the angle of the sloping bottom could be varied. This will give further insight in how the parameter $a$ in equation (6.1) will behave for different angles of the sloping bottom.

# Chapter 7

# Bibliography


[1] B. Cushman-Roisin; Introduction to Geophysical Fluid Dynamics;
Prentice-Hall Inc. Englewood Cliffs, New Jersey, 1994.

[2] G.J.F. van Heijst; Advanced Fluid Dynamics;
Syllabus, Eindhoven University of Technology, Eindhoven, 1992.[1]

[3] G.F. Carnevale, R.C. Kloosterziel and G.J.F. van Heijst;
Propagation of barotropic vortices over topography in a rotating tank;
J. Fluid Mech. 233 p.119-139, 1991.

[4] L. Zavala Sansón and G.J.F. van Heijst;
Nonlinear Ekman effects in rotating barotropic flows;
Under consideration for publication in J. Fluid Mech.; March 1999.

[5] L. Zavala Sansón and G.J.F. van Heijst;
Ekman effects in a rotating fluid with topography;
In preparation; May 1999.

[6] J.H.G.M. van Geffen; Documentation of the software package NSEVOL;
Internal report R-1466-D, Fluid Dynamics Laboratory,
Department of Applied Physics, Eindhoven University of Technology;
Eindhoven, 1998.

[7] J. Pedlosky; Geophysical Fluid Dynamics; Springer-Verlag, New York, 1987.

[8] G.J.F. van Heijst; Geophysical Fluid Dynamics;
Syllabus, Eindhoven University of Technology, Eindhoven, 1993.


[1] in Dutch

[9] S. Dalziel; DigImage, image processing for fluid dynamics;
Cambridge Environmental Research Consultants Ltd., 1995.

[10] G. van der Plas; Introduction manual for particle tracking with DigImage;
Internal report R1323-D, Eindhoven University of Technology,
Department of Applied Physics, Fluid Dynamics Laboratory, Eindhoven, 1995.

[11] R.C. Kloosterziel; Barotropic vortices in a rotating fluid;
PhD thesis; Eindhoven University of Technology, 1990.

[12] D. Hanselman and B. Littlefield; Matlab, User's guide;
Prentice Hall, Upper Saddle River, 1997.

[13] G.J.F. van Heijst; Topography effects on vortices in a rotating fluid;
Meccanica 29 p.431-451, 1994.

[14] J.R. Apel; Principles of Ocean Physics; Academic Press, London, 1987.

[15] P.K.Kundu; Fluid Mechanics; Academic Press, New York, 1990.

[16] P.W.C. Vosbeek; Contour dynamics and applications to 2D vortices;
Eindhoven University of Technology, Eindhoven 1998.

[17] R.C. Kloosterziel and G.J.F. van Heijst;
The evolution of stable barotropic vortices in a rotating free-surface fluid;
J. Fluid Mech. 239 p.607-629, 1992.

# Appendix A

# Additional figures

This appendix contains additional figures on the results of the experiments and the simulations that were done (see chapters 4 and 5). In table A.1 an overview is given of all the figures that can be found. The figure numbers are given in series of two or three, representing different water depths.

| Figure numbers | contents of figure | experiment/simulation | | |
|---|---|---|---|---|
| A.1 - A.3 | velocity fields | experiment | bottom friction | $\beta$-plane |
| A.4 - A.5 | 100 tracers | simulation | bottom friction | $\beta$-plane |
| A.6 - A.7 | vorticity fields | simulation | bottom friction | $\beta$-plane |
| A.8 - A.10 | vorticity fields | simulation | no bottom friction | $\beta$-plane |

Table A.1: *An overview of all the figures that can be found in this appendix*

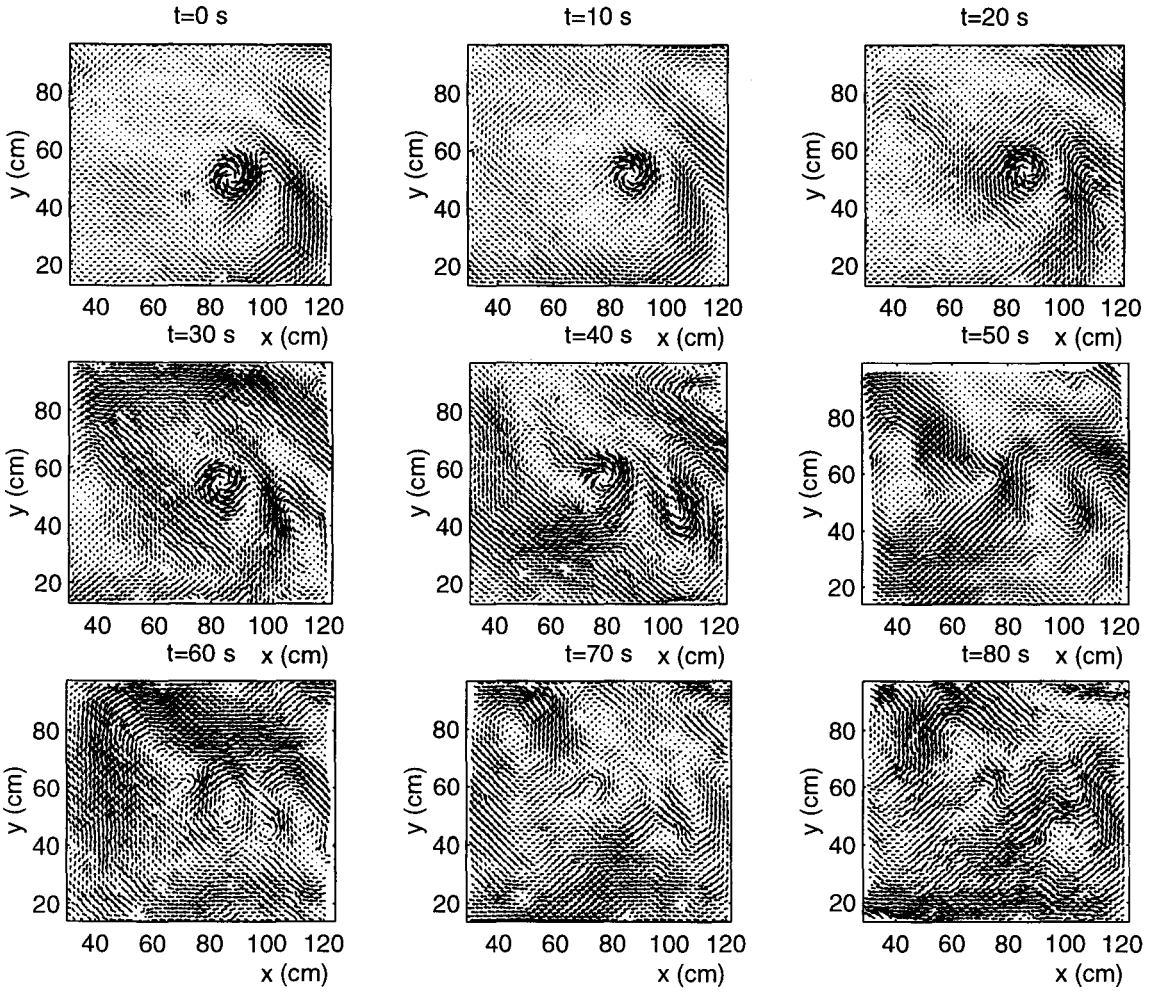


Figure A.1: *Sequence of velocity fields from experiment 1 (H=12 cm)*

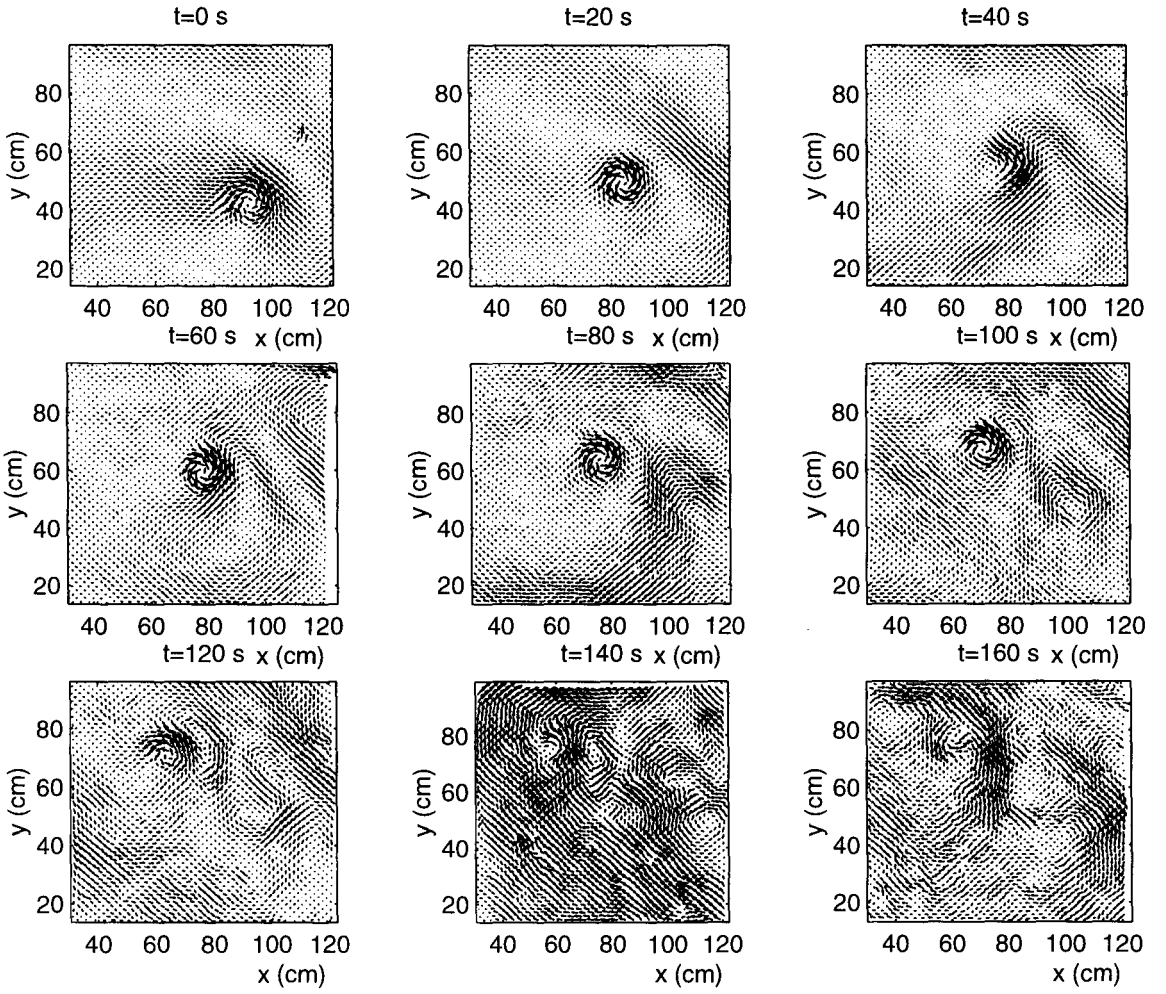


Figure A.2: *Sequence of velocity fields from experiment 2 (H=18 cm)*

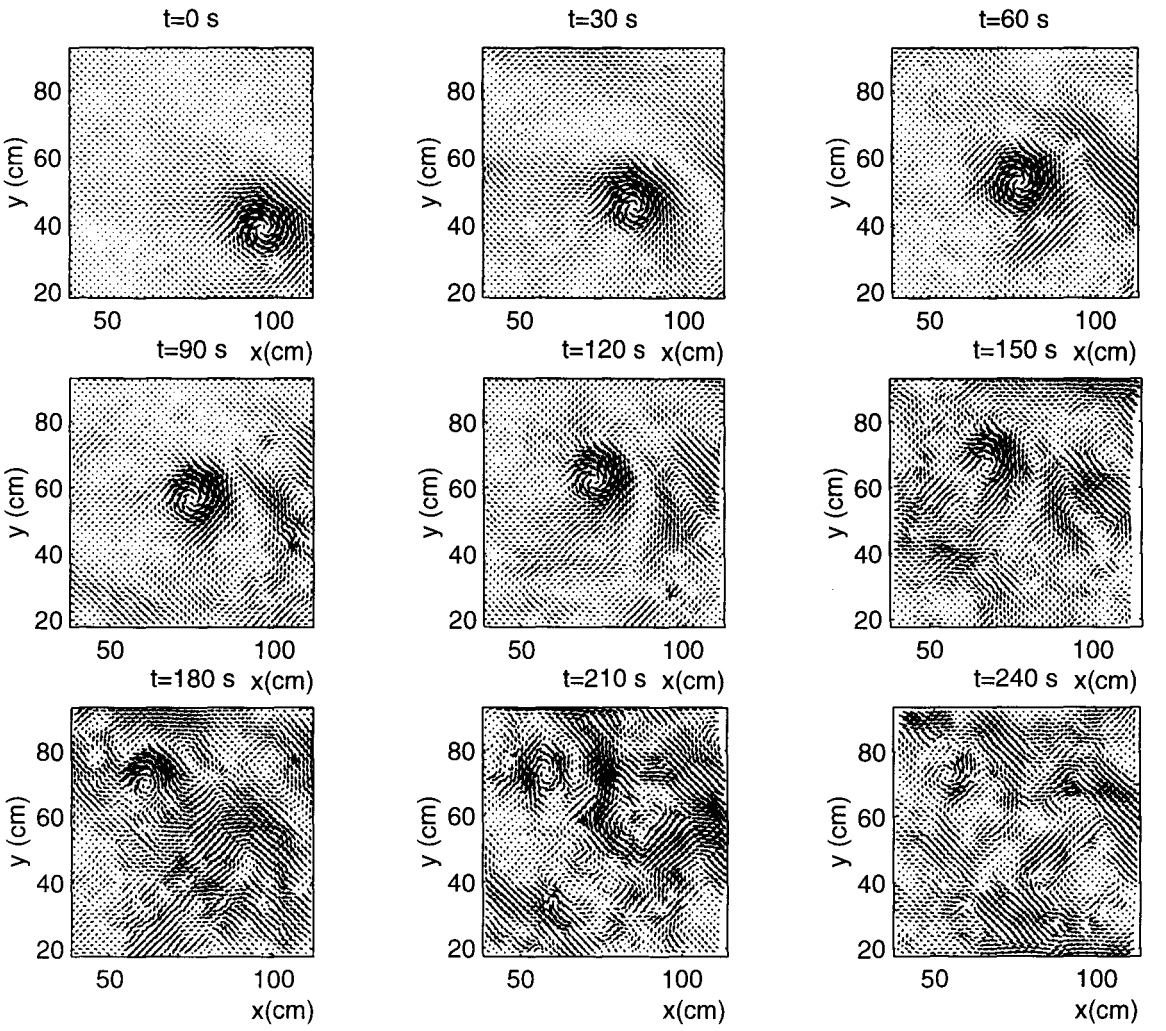


Figure A.3: *Sequence of velocity fields from experiment 3 (H=24 cm)*

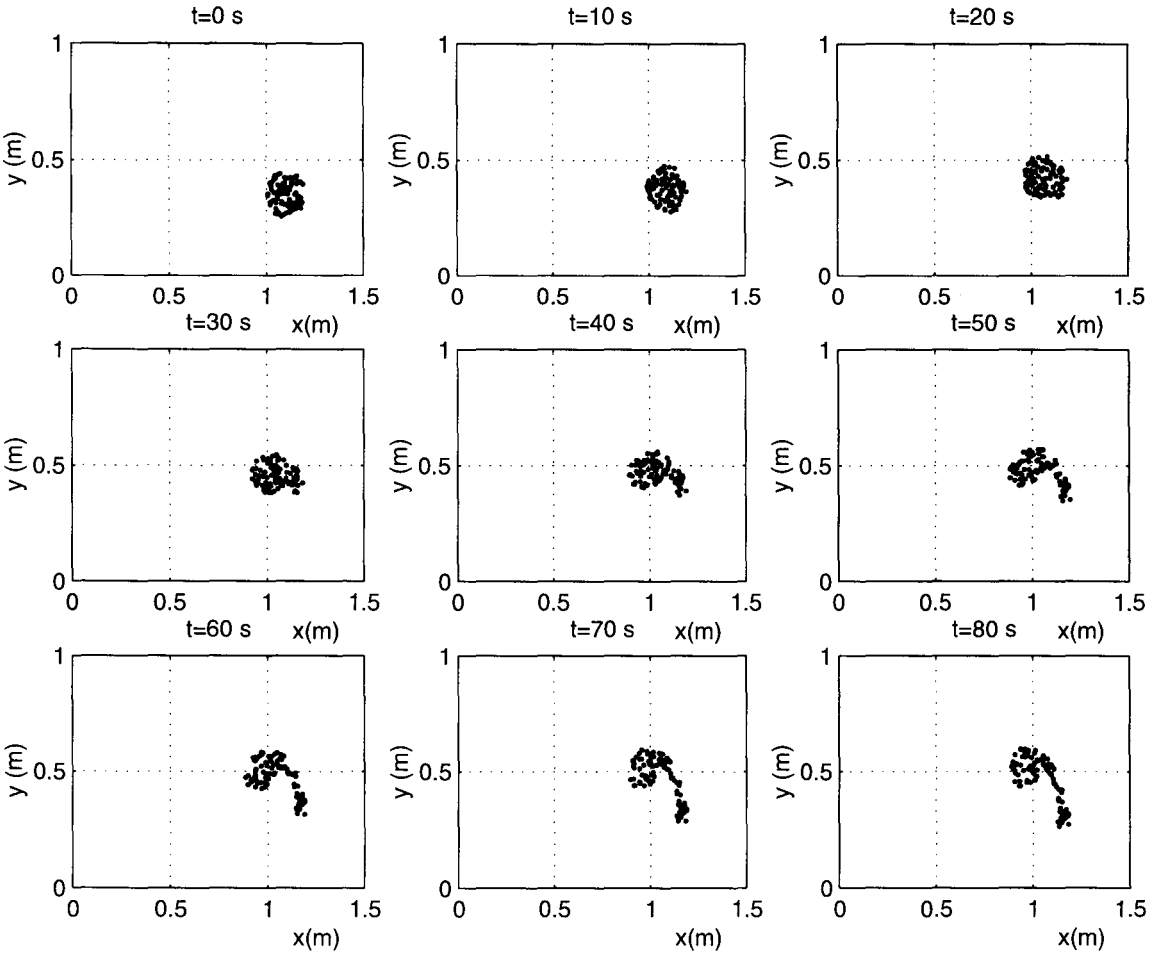


Figure A.4: *Sequence of tracer positions for the simulation on a $\beta$-plane, including bottom friction due to Ekman layers, for the case of H=12 cm. 100 tracers were randomly put in the initially circular monopolar vortex. Some of the tracers are leaking out of the (core of) the vortex, indicating that the vortex is releasing fluid to the ambient.*

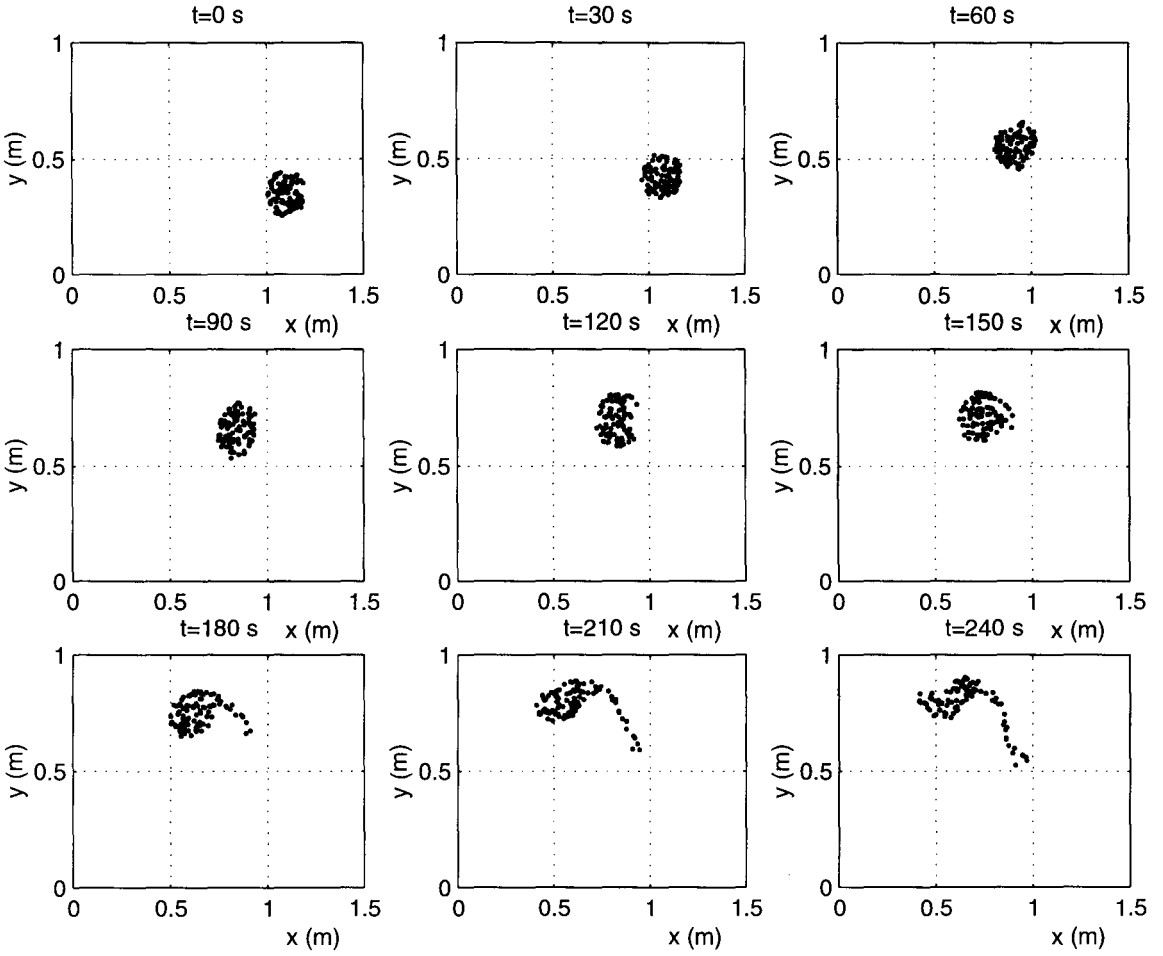


Figure A.5: *Sequence of tracer positions for the simulation on a $\beta$-plane, including bottom friction due to Ekman layers, for the case of H=24 cm. 100 tracers were randomly put in the initially circular monopolar vortex. Some of the tracers are leaking out of the (core of) the vortex, indicating that the vortex is releasing fluid to the ambient.*

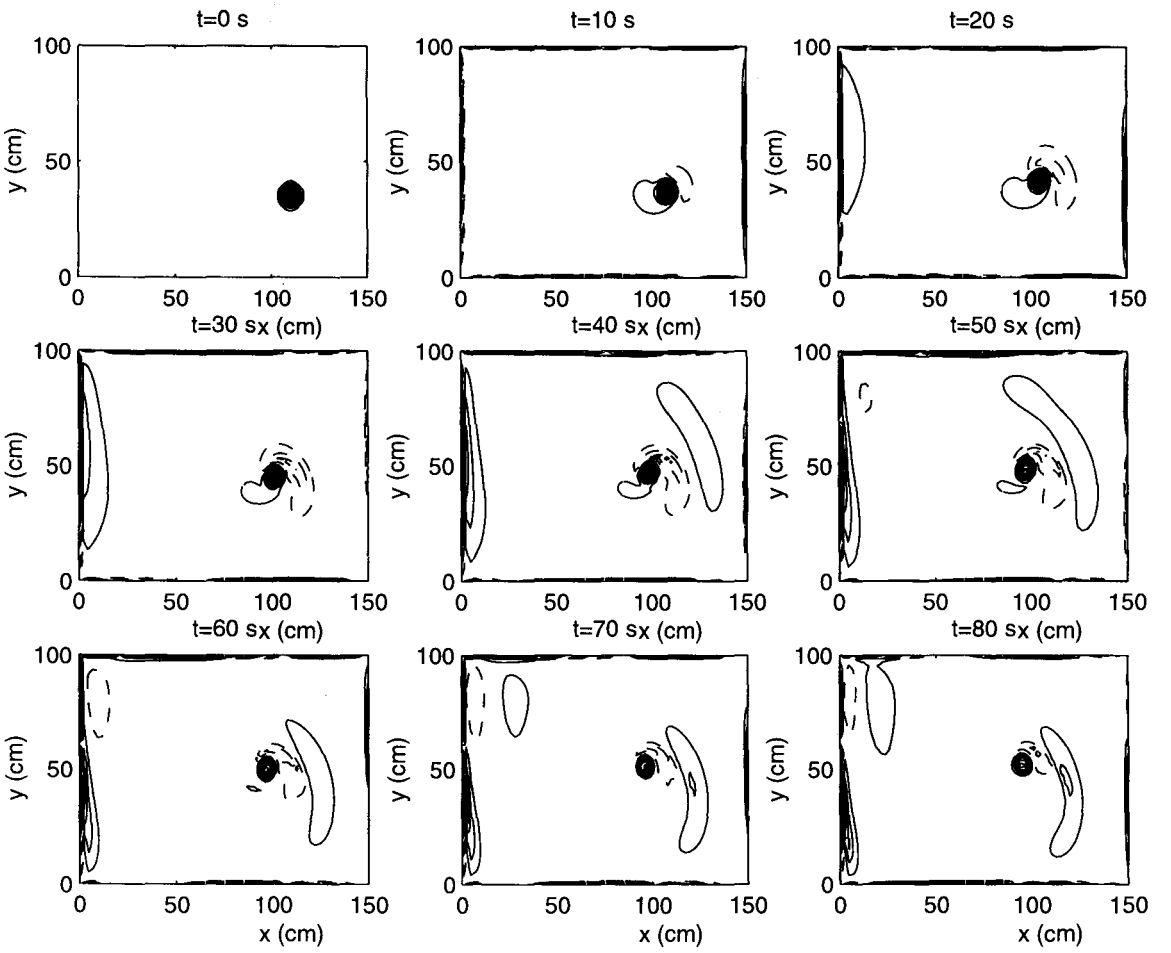


Figure A.6: *Sequence of vorticity contours from the simulation on a $\beta$-plane, including bottom friction due to Ekman layers, for the case of H=12 cm. The interval between two contours is 0.05 $s^{-1}$. The solid lines indicate positive vorticity and the dashed lines indicate negative vorticity. The formation of Rossby waves can clearly be seen: first an induced cell with negative vorticity appears and then a second induced cell with positive vorticity also appears.*

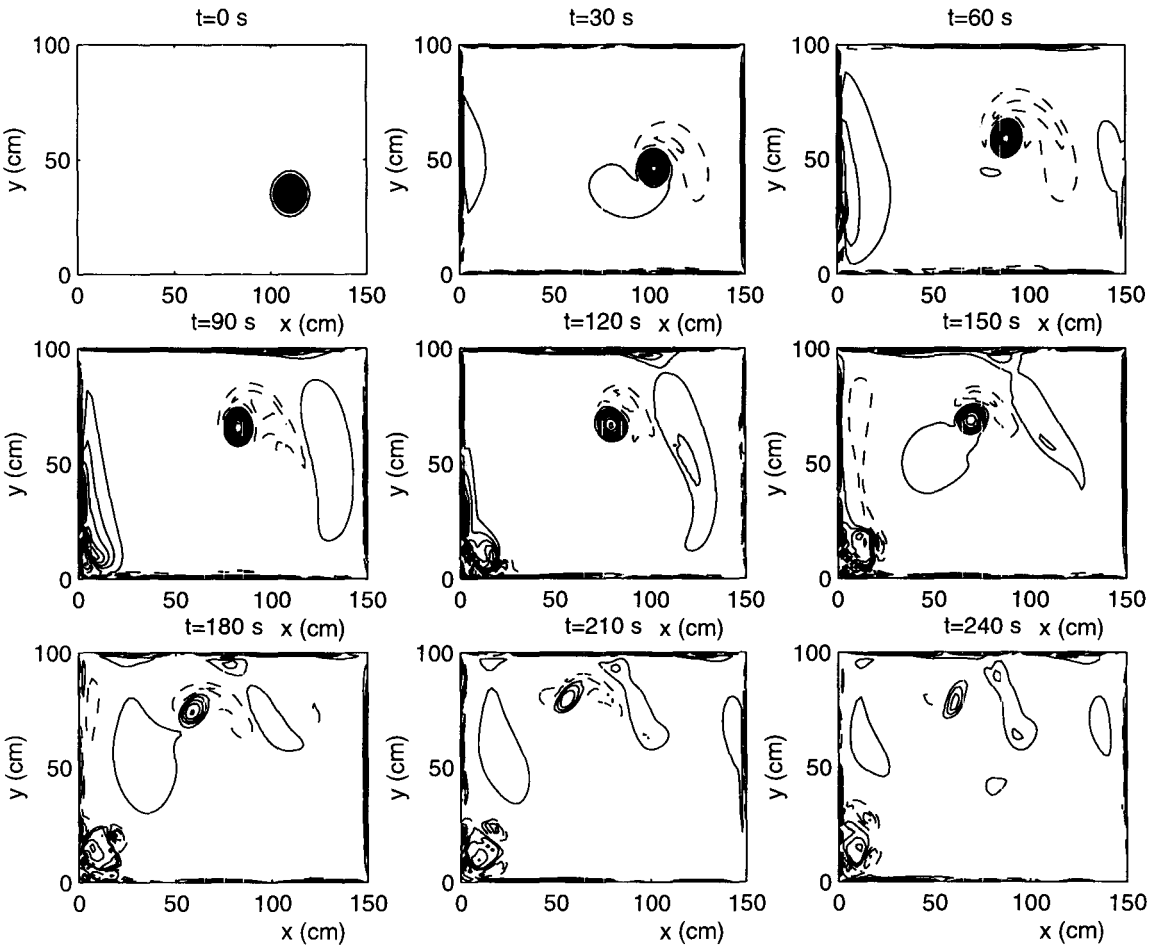


Figure A.7: *Sequence of vorticity contours from the simulation on a $\beta$-plane, including bottom friction due to Ekman layers, for the case of H=24 cm. The interval between two contours is 0.05 $s^{-1}$. The solid lines indicate positive vorticity and the dashed lines indicate negative vorticity. The formation of Rossby waves can clearly be seen: first an induced cell with negative vorticity appears and then a second induced cell with positive vorticity also appears.*

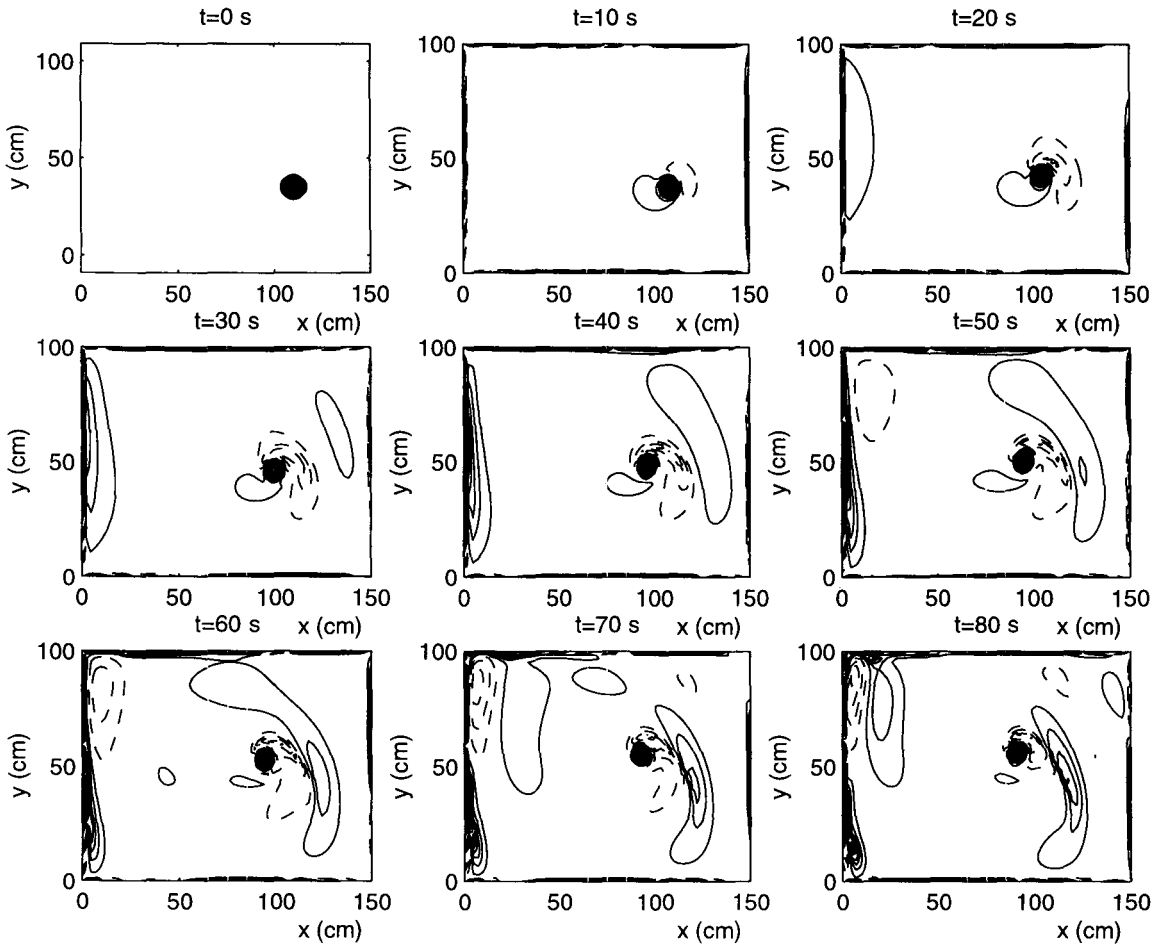


Figure A.8: *Sequence of vorticity contours from the simulation on a $\beta$-plane, without including bottom friction due to Ekman layers, for the case of H=12 cm. The interval between two contours is 0.05 $s^{-1}$. The solid lines indicate positive vorticity and the dashed lines indicate negative vorticity. The formation of Rossby waves can clearly be seen: first an induced cell with negative vorticity appears and then a second induced cell with positive vorticity also appears.*

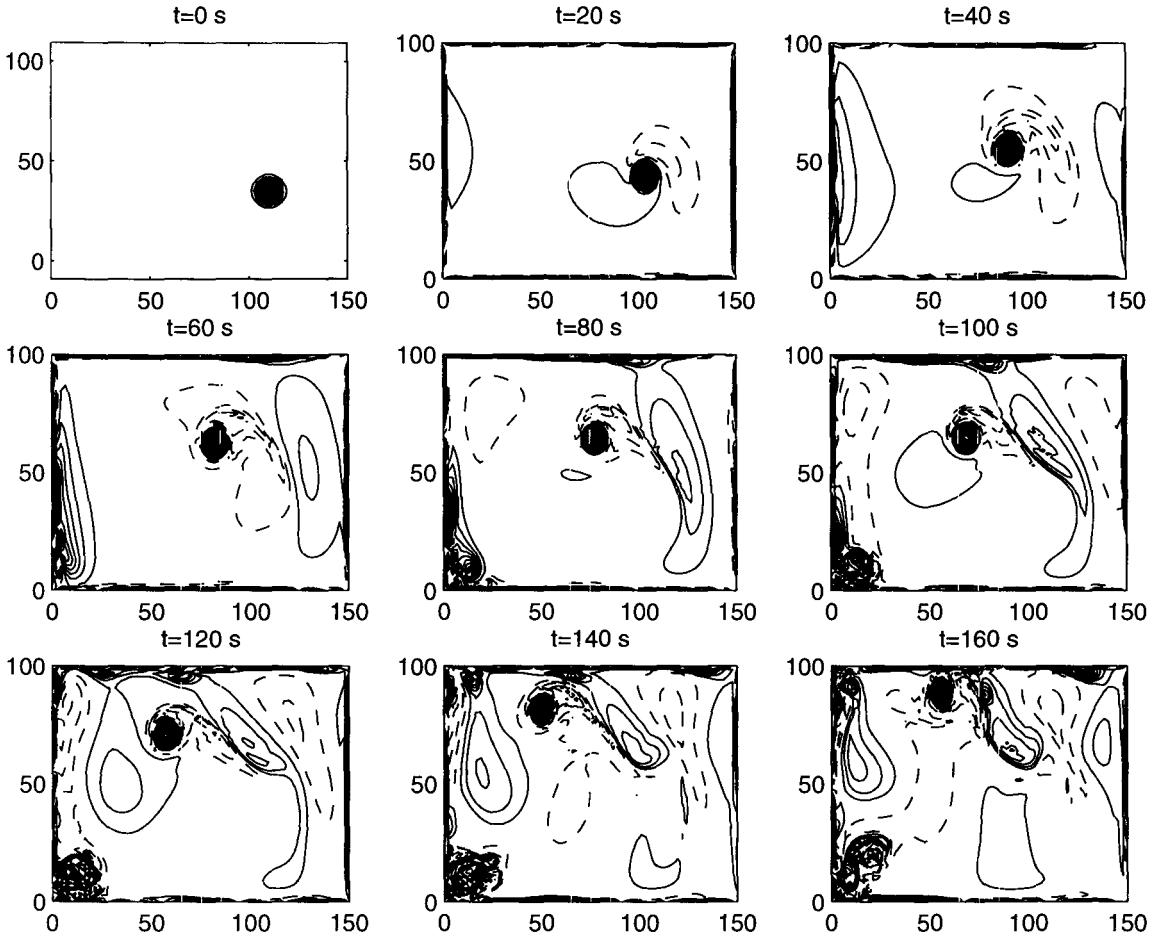


Figure A.9: *Sequence of vorticity contours from the simulation on a $\beta$-plane, without including bottom friction due to Ekman layers, for the case of H=18 cm. The interval between two contours is 0.05 $s^{-1}$. The solid lines indicate positive vorticity and the dashed lines indicate negative vorticity. The formation of Rossby waves can clearly be seen: first an induced cell with negative vorticity appears and then a second induced cell with positive vorticity and a third induced cell with negative vorticity also appear.*

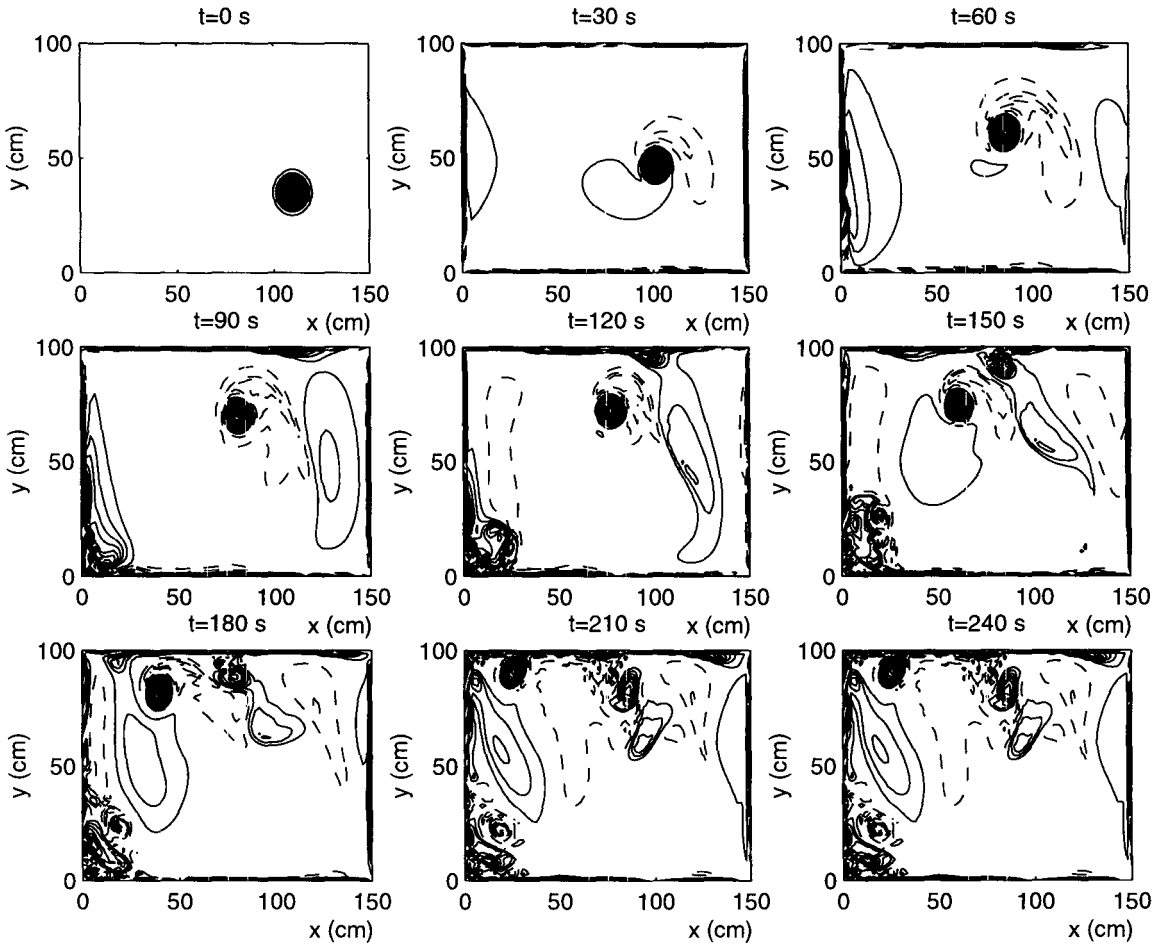


Figure A.10: *Sequence of vorticity contours from the simulation on a $\beta$-plane, without including bottom friction due to Ekman layers, for the case of H=24 cm. The interval between two contours is 0.05 $s^{-1}$. The solid lines indicate positive vorticity and the dashed lines indicate negative vorticity. The formation of Rossby waves can clearly be seen: first an induced cell with negative vorticity appears and then a second induced cell with positive vorticity and a third induced cell with negative vorticit also appear.*

# Appendix B

# Nonlinear Ekman effects

In this appendix equations (2.46) and (2.47) will be derived. This model is a two-dimensional formulation for rotating barotropic flows over a variable topography. Ekman effects, associated to the no-slip boundary condition at the solid bottom, are also incorporated. The model applies for low to moderate Rossby numbers and smoothly-varying bottom topographies. The derivation is taken from [5].

Consider the vorticity equation (2.35):

$$\frac{\partial \zeta}{\partial t} + u\frac{\partial \zeta}{\partial x} + v\frac{\partial \zeta}{\partial y} + \left(\frac{\partial u}{\partial x} + \frac{\partial v}{\partial y}\right)(\zeta + f) = \nu \nabla^2 \zeta \tag{B.1}$$

and the continuity equation

$$\frac{\partial u}{\partial x} + \frac{\partial v}{\partial y} + \frac{\partial w}{\partial z} = 0 \tag{B.2}$$

where it is assumed that $u$ and $v$ are independent of $z$. Integration of the continuity equation over the fluid depth, i.e. from $z = h_B$ to $z = h$, yields:

$$\left(\frac{\partial u}{\partial x} + \frac{\partial v}{\partial y}\right) H = -[w(z = h) - w(z = h_B)] \tag{B.3}$$

Ignoring the wind stress, the vertical velocity on the free surface is given by:

$$w(z = h) = \frac{dh}{dt} \tag{B.4}$$

with d/dt the material derivative, given by equation (2.15). For a variable topography the Ekman condition (equation (2.34)) becomes [7]:

$$w(z = h_B) = \underline{v} \cdot \nabla h_B + \frac{1}{2} d_E \zeta \tag{B.5}$$

with $d_E$ the physical thickness of the Ekman layer, given by $d_E = H\sqrt{E}$. Note that the first part of the Ekman condition, $\underline{v} \cdot \nabla h_B$ expresses the vertical velocity induced by the shape

of the topography, which is zero for a flat bottom. Using (B.4) and (B.5), the horizontal divergence in (B.3) may be written as:

$$\frac{\partial u}{\partial x} + \frac{\partial v}{\partial y} = -\frac{1}{H}\frac{dH}{dt} + \frac{d_E}{2H}\zeta \tag{B.6}$$

This expression states that the horizontal divergence is caused by changes in the fluid depth and by the vertical velocity induced by the Ekman layer at the bottom. Assuming that the free-surface elevations are much smaller than the topographic variations, the time derivative can be filtered out in equation (B.6):

$$\frac{\partial u}{\partial x} + \frac{\partial v}{\partial y} = -\frac{1}{H}\left(u\frac{\partial H}{\partial x} + v\frac{\partial H}{\partial y}\right) + \frac{d_E}{2H}\zeta \tag{B.7}$$

Substitution of (B.7) in (B.1) results in:

$$\frac{\partial \zeta}{\partial t} + Hu\frac{\partial \omega_p}{\partial x} + Hv\frac{\partial \omega_p}{\partial y} = \nu\nabla^2\zeta - \frac{d_E}{2H}\zeta(\zeta + f) \tag{B.8}$$

with $\omega_p$ the potential vorticity given by equation (2.44).

Now a stream function $\psi_p$ is defined, from (B.7):

$$\begin{cases} Hu - \frac{1}{2}d_E v = \dfrac{\partial \psi_p}{\partial y} \\ Hv + \frac{1}{2}d_E u = -\dfrac{\partial \psi_p}{\partial x} \end{cases} \tag{B.9}$$

From these equations, expressions for the velocities in terms of the stream function can be derived. Assuming that the Ekman layer thickness is always much smaller than the fluid depth, i.e. $(d_E/2H)^2 \ll 1$, these expressions are:

$$u = \frac{1}{H}\left(\frac{\partial \psi_p}{\partial y} - \frac{d_E}{2H}\frac{\partial \psi_p}{\partial x}\right) \tag{B.10}$$

$$v = \frac{1}{H}\left(-\frac{\partial \psi_p}{\partial x} - \frac{d_E}{2H}\frac{\partial \psi_p}{\partial y}\right) \tag{B.11}$$

By substitution of equation (B.10) and (B.11) in the definition of the relative vorticity (equation (2.14)) it is verified that:

$$\zeta = -\frac{1}{H}\nabla^2\psi_p + \frac{1}{H^2}\nabla H \cdot \nabla\psi_p + \frac{d_E}{2H}\frac{2}{H^2}J(H, \psi_p) \tag{B.12}$$

Finally the evolution equation for the relative vorticity is obtained by inserting (B.10) and (B.11) in (B.8):

$$\frac{\partial \zeta}{\partial t} + J(\omega_p, \psi_p) - \frac{d_E}{2H}\nabla\psi_p \cdot \nabla\omega_p = \nu\nabla^2\zeta - \frac{d_E}{2H}\zeta(\zeta + f) \tag{B.13}$$

# Appendix C

# Technology assessment

The field of geophysical fluid dynamics concerns the behaviour of large-scale flows in the atmosphere and the oceans of the Earth. These large-scale flows are approximately two-dimensional and very persistent, i.e. they have long lifetimes. Coherent vortex structures are common features of quasi-geostrophic or two-dimensional flows. In the oceans and in the atmosphere, vortices are abundant.

The importance of this subject lies in a variety of applications: e.g. the prediction of the paths of hurricanes, the advection of pollutants in the atmosphere and the understanding of periodic passage of warm water along the tropical Pacific and the western coast of South America. To be more concretely, illustrating examples of recent phenomena are: the northwards deviation of hurricane Floyd towards the east coast of the United States, the spreading of radioactive elements after the Chernobyl catastrophe and the well-known El Niño effect. Atmospheres of other planets also show the occurrence of long-lived vortex structures. An illustrating example of this is the Great Red Spot on Jupiter.